Available online at www.sciencedirect.com

ScienceDirect

Geochimica et Cosmochimica Acta 212 (2017) 62–83

Geochimica et Cosmochimica Acta

www.elsevier.com/locate/gca

The effect of melt composition on metal-silicate partitioning of siderophile elements and constraints on core formation in the angrite parent body

E.S. Steenstra [a,*], A.B. Sitabi [a], Y.H. Lin [a], N. Rai [b,c], J.S. Knibbe [a], J. Berndt [d], S. Matveev [e], W. van Westrenen [a]

[a] Faculty of Earth and Life Sciences, VU University Amsterdam, Amsterdam, The Netherlands
[b] Centre for Planetary Sciences, Birkbeck University of London, London, UK
[c] Department of Earth Sciences, Mineral and Planetary Sciences Division, Natural History Museum, London, UK
[d] Department of Mineralogy, University of Münster, Germany
[e] Department of Petrology, Utrecht University, The Netherlands

Received 8 December 2016; accepted in revised form 26 May 2017; available online 1 June 2017

Abstract

We present 275 new metal-silicate partition coefficients for P, S, V, Cr, Mn, Co, Ni, Ge, Mo, and W obtained at moderate P (1.5 GPa) and high T (1683–1883 K). We investigate the effect of silicate melt composition using four end member silicate melt compositions. We identify possible silicate melt dependencies of the metal-silicate partitioning of lower valence elements Ni, Ge and V, elements that are usually assumed to remain unaffected by changes in silicate melt composition. Results for the other elements are consistent with the dependence of their metal-silicate partition coefficients on the individual major oxide components of the silicate melt composition suggested by recently reported parameterizations and theoretical considerations. Using multiple linear regression, we parameterize compiled metal-silicate partitioning results including our new data and report revised expressions that predict their metal-silicate partitioning behavior as a function of P-T-X-fO_2. We apply these results to constrain the conditions that prevailed during core formation in the angrite parent body (APB). Our results suggest the siderophile element depletions in angrite meteorites are consistent with a CV bulk composition and constrain APB core formation to have occurred at mildly reducing conditions of 1.4 ± 0.5 log units below the iron-wüstite buffer (ΔIW), corresponding to a APB core mass of $18 \pm 11\%$. The core mass range is constrained to 21 ± 8 mass% if light elements (S and/or C) are assumed to reside in the APB core. Incorporation of light elements in the APB core does not yield significantly different redox states for APB core-mantle differentiation. The inferred redox state is in excellent agreement with independent fO_2 estimates recorded by pyroxene and olivine in angrites.

Keywords: Angrite; Accretion; Core; Metal; Silicate; Siderophile

1. INTRODUCTION

Geochemical planetary differentiation models derive estimates of core formation conditions from siderophile element abundances in planetary mantles. Siderophile elements exhibit a preference for Fe-metal and their partitioning between metal and silicate is controlled by pressure (P), temperature (T), composition of metal and silicate (X) and oxygen fugacity (fo_2) (e.g., Walter et al., 2000; Righter, 2003). Depletion patterns of siderophile elements in planetary mantles are used to derive conditions at which

* Corresponding author.
E-mail address: e.s.steenstra@vu.nl (E.S. Steenstra).

http://dx.doi.org/10.1016/j.gca.2017.05.034
0016-7037/

liquid metal and liquid silicate equilibrated during core formation, by comparison of their depletions with their experimentally determined metal-silicate partitioning behavior as a function of *P-T-X-f*O_2. This approach has been applied to smaller-sized bodies including the Moon (Rai and van Westrenen, 2014; Steenstra et al., 2016a, 2017a), asteroid 4-Vesta (Righter and Drake, 1996; Holzheid and Palme, 2007; Steenstra et al., 2016b) and the angrite parent body (APB) (Righter, 2008; Shirai et al., 2009; van Westrenen et al., 2016). However, the outcome of these models relies heavily on the accuracy of equations that predict the metal-silicate partition coefficients of siderophile elements as a function of *P-T-X-fO*$_2$ (Palme et al., 2011; Walter and Cottrell, 2013; Rai and van Westrenen, 2014).

Previous studies have shown that metal-silicate partitioning of siderophile elements including P, Ga, Mo, and W may be strongly dependent on the composition of the silicate melt (Hillgren et al., 1996; Jana and Walker, 1997a,b; Righter et al., 1997; Walter et al., 2000; Righter, 2003; Righter, 2011a,b; Steenstra et al., 2016c). To date, few studies presented experimental results performed at isobaric and isothermal conditions to isolate the effects of silicate melt composition on D. As a result, experimental studies often yield different, sometimes contradictory dependencies of D on silicate melt composition. For example, Righter (2011a) report a strong positive dependency of D(P) on the four silicate melt major oxide components MgO, SiO_2, CaO, and FeO, whereas Rai and van Westrenen (2014) report predominantly strongly negative dependencies. Another example is the heated debate about whether the metal-silicate partitioning of Ni and Co is dependent or independent of silicate melt composition (Palme et al., 2011; Righter, 2011a,b). Most of the currently published low pressure metal-silicate partitioning data was obtained for silicate melts that were relatively low in FeO (<15 wt. %) and high in MgO (>25 wt.%), relevant for core formation in reduced bodies (e.g., Siebert et al., 2011). As a consequence, it is possible that current parameterizations do not fully account for silicate melt compositional effects on metal-silicate partition coefficients. This could affect the outcome of geochemical models of core formation in more oxidized bodies, such as the angrite parent body (APB).

This study assesses the effects of MgO, FeO, and other major silicate melt compositional parameters on the metal-silicate partitioning of siderophile elements that are most commonly used in geochemical models of core formation. We compare and contrast experimentally determined D values using four end-member silicate melt compositions (with low versus high MgO, CaO and SiO_2). The data are then used to provide improved parameterizations for predicting D, which are used to study core formation in the APB.

Angrites are a diverse suite of relatively oxidized, volcanic-plutonic and mafic achondrites that are thought to have been derived from a differentiated asteroidal parent body. Differentiation of the angrite parent body (APB) is suggested from W isotope systematics (Kleine et al., 2012), evidence for an early core dynamo based on magnetic field data (Weiss et al., 2008) and the depletion of a number of siderophile elements (Ga, Co, Ni, Sb, Mo, W) (Righter, 2008; Shirai et al., 2009) relative to its presumed chondritic building blocks. However, there is still considerable debate about the interior structure of the APB, including its core mass and composition. In addition, the extent of melting during core formation and the prevailing redox conditions are poorly constrained. Some authors argue for the existence of a magma ocean on the APB, based on the relatively homogenous $\Delta^{17}O$ isotope signature of angrites that implies large-scale homogenization in a convecting magma ocean (e.g., Greenwood et al., 2005; Sugiura et al., 2005). Indeed, the crystallization ages of angrites are within the range where ^{26}Al-^{26}Mg would be a major heat producing source, which is expected to result in efficient melting and metal-silicate segregation (Schiller et al., 2015). However, Kleine et al. (2012) suggest that core formation in the APB was not a single metal-silicate equilibration event. They argue for a multi-step core formation model, based on the existence of distinct Hf-W source ages. These distinct age groups may also be explained by late crystallization of kamacite and tetrataenite, as inferred from angrite NWA 4801 (Riches et al., 2012) and/or post-core formation addition of variable amounts of exogenous iron-rich impactors (Baghdadi et al., 2015). Using our new data we investigate the redox conditions that prevailed during core formation in the APB and aim to further constrain its physical properties (e.g., core mass).

2. METHODS

2.1. Experimental techniques

Experiments were performed using silicate mixtures of high-purity powdered oxides and carbonates representing synthetic analogues of the Apollo 14B black glass (Delano, 1986), Apollo 15C green glass (Delano, 1986), a typical lunar granite (Warren et al., 1983) and a terrestrial basaltic composition (KB) (Appendix Section A.1). These four silicate melt compositions provide compositional end members in terms of SiO_2, TiO_2, MgO and CaO, and were chosen to better constrain silicate melt compositional effects on D and improve current parameterizations that predict D. Metal powder mixtures were prepared by doping high-purity Fe metal powder with 1.5 wt.% of siderophile elements Ni, Co, Mo, Ge, W, V and various amounts of FeS to generate between 0 and 15 wt.% of S upon melting, spanning current estimates of the S content of planetary cores in the solar system (Table 1). Details of the preparation of the starting materials are provided in the Appendix Section A.1.

Experiments were conducted in polycrystalline MgO (3 mm O.D., 1.5 mm I.D., 4 mm long) capsules and mixtures were loaded in a 2:1 silicate:metal ratio by weight. Experimental conditions varied between 1683 and 1883 K at a constant pressure of 1.5 GPa and were performed in an end-loaded piston cylinder press (Boyd and England, 1960) in the high-pressure laboratory at Vrije Universiteit, Amsterdam. All of the experiments used a 13 mm O.D. talc-Pyrex pressure cell assembly, which consisted of concentric sleeves of (outer) natural talc, (inner) Pyrex glass, a graphite furnace and a Al_2O_3 crushable sleeve spacer

Table 1
Experimental run conditions and products (all runs performed in MgO capsules at 1.5 GPa).

Run #	Comp[a]	T (K)	t (min)	ΔIW[b]	ΔIW[c]
GGS–1	GG + 0% S	1783	15	−1.11	−1.11
GGS–2	GG + 2% S	1783	15	−1.41	−1.41
GGS–3	GG + 2% S	1783	15	−1.27	−1.27
GGS–4	GG + 4% S	1783	15	−1.13	−1.13
GGS–5	GG + 6% S	1783	15	−0.92	−0.92
GGS–6	GG + 6% S	1783	30	−1.01	−1.02
GGS–9	GG + 10% S	1783	15	−1.46	−1.46
GGS–10	GG + 10% S	1783	15	−1.21	−1.21
GGS–11	GG + 10% S	1783	15	−1.23	−1.23
GGS–12	GG + 10% S	1783	15	−1.06	−1.06
GGS–16	GG + 8% S	1883	15	−1.27	−1.28
GGS–18	GG + 10% S	1883	15	−1.19	−1.17
LGS–4	LG + 6% S	1683	15	−1.88	−1.88
LGS–5	LG + 6% S	1683	30	−1.32	−1.33
LGS–7	LG + 8% S	1683	15	−1.35	−1.37
LGS–11	LG + 8% S	1883	15	−1.75	−1.76
LGS–12	LG + 10% S	1883	120	−2.53	−2.53
LGS–13	LG + 10% S	1883	60	−1.65	−1.66
LGS–14	LG + 15% S	1883	60	−1.95	−2.00
LGS–15[d]	LG + 15% S	1883	60	−2.17	−2.15
LGS–16	LG + 0% S	1883	60	−1.95	−1.95
LGS–17	LG + 0% S	1883	30	−1.87	−1.87
KB–1	KB + 10% S	1883	30	−1.58	−1.60
KB–2	KB + 10% S	1883	30	−1.74	−1.78
KB–3	KB + 15% S	1883	60	−2.18	−2.20
KB–4	KB + 0% S	1883	60	−2.14	−2.14
KB–5	KB + 0% S	1883	60	−2.49	−2.49
KB–6	KB + 15% S	1883	60	−2.39	−2.40
BG–1	BG + 10% S	1883	30	−1.18	−1.19
BG–2	BG + 0% S	1883	60	−1.53	−1.54
BG–4	BG + 0% S	1883	30	−1.41	−1.41

[a] GG: Apollo 15 green glass; LG: lunar granite; KB: Knippa basalt; BG: Apollo 14 black glass.
[b] Assuming ideal mixing behavior of Fe.
[c] Assuming non-ideal mixing behavior of Fe.
[d] Metal consisted of S-poor and S-rich metal phases.

(van Kan Parker et al., 2011). Pressure calibration was based on the fayalite + quartz = ferrosillite and albite = jadeite + quartz equilibria (van Kan Parker et al., 2011) resulting in a friction correction of <3% and a pressure uncertainty of 0.1 GPa, consistent with literature data on comparable assemblies (McDade et al., 2002). Temperatures were measured and controlled using a type "D" W-Re (W_{97}-Re_3 - W_{75}-Re_{25}) thermocouple contained in a four bore alumina sleeve, which was placed on top of a thin (0.6 mm) ruby disc on top of the sample capsule. Due to the increased distance of the thermocouple tip to the sample reported temperatures are adjusted 10 K upwards from the thermocouple readings (Wood et al., 2014). Samples were first heated at a rate of 100 K/min to 1073 K. At 1073 K, the samples were sintered for 60 min to reduce the porosity and permeability of the MgO capsule. Samples were then heated at a rate of 100 K/min to the intended peak temperatures (Table 1). Pressure was gradually increased during heating (hot piston-in technique). Run times were kept relatively short (<120 min) to minimize sample - capsule wall interaction and to minimize loss of Ni and Co (Tuff et al., 2011). To ensure equilibrium metal-silicate partitioning, run times of >15 min were used that have been previously shown to be sufficient for attaining equilibrium for similar capsule dimensions and *P-T* conditions (e.g., Kiseeva and Wood, 2013; Steenstra et al. 2016c; Appendix Section A.5). After the desired run time, experiments were rapidly quenched by shutting off the power to the furnace, while simultaneously maintaining pressure. The recovered samples were mounted in petropoxy resin, sectioned perpendicular to the long axis of the capsule and fine polished using <1 μm diameter diamond grains for electron microprobe and LA-ICPMS analyses.

Typical run products (Fig. 1) consisted of large spherical blobs (<400 μm diameter) of Fe-rich metallic alloys embedded in a quenched silicate. The silicates show typical skeletal-shaped quench crystals embedded in interstitial glass. Compositions that were initially poor in MgO showed a significant increase of MgO, which reflects reaction with the surrounding capsule walls (Thibault and Walter, 1995; Hillgren et al., 1996; Killburn and Wood, 1997; Tuff et al., 2011). The metal is composed of S-rich and S-poor immiscible phases and shows a variety of exsolution- and quench textures (Fig. 1), similar to those observed by e.g. Blanchard et al. (2015), confirming the liquid state of the metal upon quenching.

2.2. Analytical techniques

Samples were analyzed for metal and silicate major element abundances with a JEOL JXA 8800M Electron Microprobe at Vrije Universiteit Amsterdam or a JXA JEOL 8530F field emission electron probe microanalyser at the Dutch National Geological Facility at Utrecht University (Tables 2 and 3). Metal and silicate phases were analyzed with a defocused beam of which the diameter was roughly equivalent to the step size, ranging between 5 and 15 μm, using a beam current of 20 nA and an accelerating voltage of 15 kV. Where possible, at least 25 repeat analyses were performed for the metal and silicate portions in each charge and care was taken to avoid analyzing the reaction rims close to the capsule walls or areas close the edge of each phase (e.g., Wood et al., 2014). Counting times were as follows: 30 s peak and 15 s background for major elements (Si, Al, Ti, Cr, Ga, Mg, Fe, Mn), 20 s peak and 10 s background for minor elements (P, W, V, S, Mo, Ge, Ga, Co, Ni).

Metal standards were $KTiPO_5$ for P, tephroite for Mn, chalcopyrite for S and pure metal standards for V, Cr, Fe, Co, Ni, Ge, Mo and W. Silicate analyses were calibrated with diopside for Si and Ca, forsterite for Mg, corundum for Al, hematite for Fe, tephroite for Mn, $KTiPO_5$ for P and K, TiO for Ti, jadeite for Na, chalcopyrite for S and pure metal standards for Cr and Ge, V, W, Co, Ni, Mo. Data reduction was performed using the Φ (rZ) correction (Armstrong, 1995). The instrument calibration was deemed successful when the composition of secondary standards was reproduced within the error margins defined by the counting statistics.

Some of the trace element abundances in the silicate (Ni, Co, Mo, Ge, W) and metal (V, Cr, Mn) were close to or below electron microprobe detection limits. Laser ablation

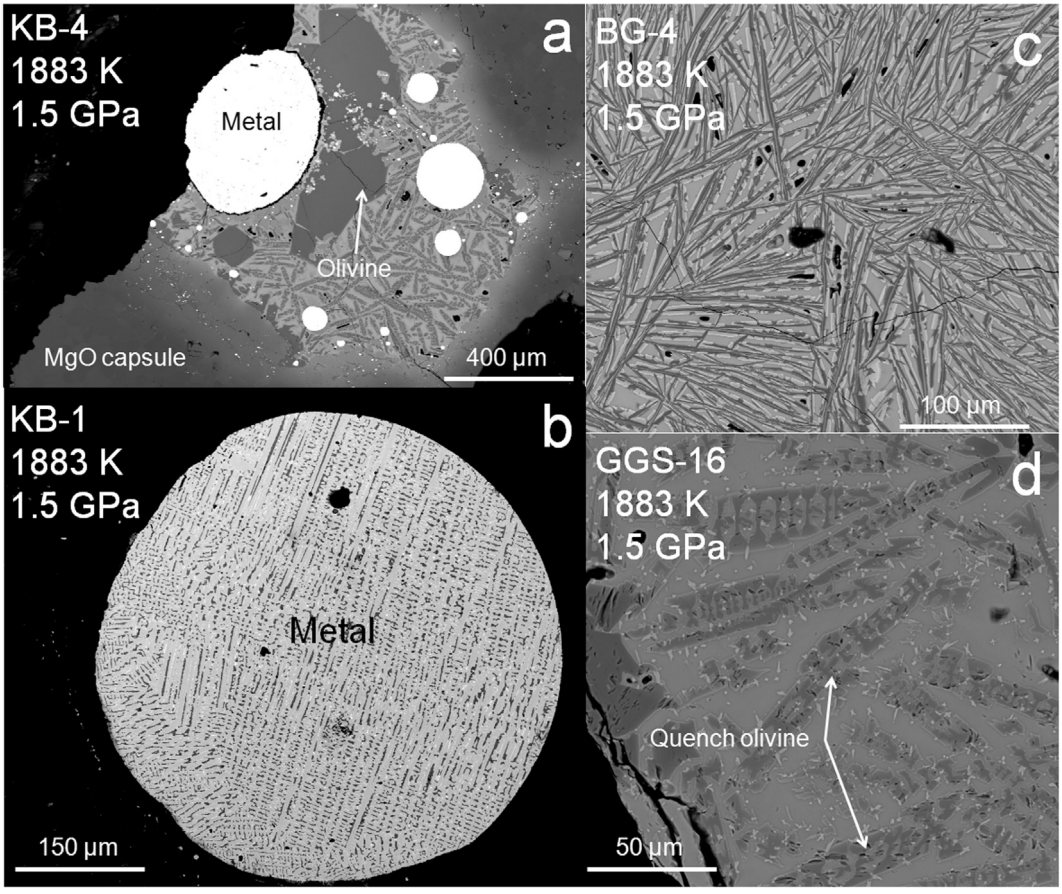

Fig. 1. Backscattered electron images of typical run products. Panel (a) shows the distinct separation between metallic blobs (bright white) and quenched silicate (grey). Both the metal and silicate show clear quench textures, confirming their liquid state upon quenching (b–d).

inductively coupled mass spectrometry (LA-ICPMS) was therefore used to measure their abundances (Tables 2 and 3). Sample ablation was performed with a pulsed 193 nm ArF excimer laser (Analyte G2, Photon Machines) at the University of Münster, using a repetition rate of 10 Hz and an energy of ~3–4 J/cm^2 throughout the entire session. Beam sizes varied between 25 and 50 µm. The following isotopes were measured: ^{29}Si, ^{47}Ti, ^{51}V, ^{53}Cr, ^{55}Mn, ^{59}Co, ^{60}Ni, ^{72}Ge, ^{95}Mo, and ^{182}W, with yields calibrated on the NIST 612 glass standard as primary standard. To monitor the accuracy of the NIST 612 calibration, Hoba, Arispe, Tocopilla and Campo del Cielo iron meteorites were used as secondary standards for the metals, while two USGS basaltic glass standards (BCR-2G, BIR-1G) were used for silicates. To monitor the accuracy of the calibration, the NIST 612 calibration was checked every 50 analyses for metals and every 20 analyses for silicates. Internal standards for metal and silicate phases were Ni and Si, respectively, as previously determined by electron microprobe analysis. Data reduction was performed using GLITTER software (van Achterbergh et al., 2001; Griffin et al., 2008) and included monitoring and/or identification of heterogeneities (e.g., metal inclusions in silicate) or vertical compositional variation.

A full comparison of our analyses with recommended/published values of the silicate and metal external standards is provided in Appendix Section A.2. We observe that for all standards our results agree well with recommended and/or literature values. However, the measured metal major element abundances (>1 wt.%) obtained with LA-ICPMS show a systematic offset compared to values obtained by electron microprobe analysis. This is probably a consequence of incomplete ablation of refractory elements (e.g., Wood et al. 2014), which is substantiated by the excellent agreement between trace elements abundances (<300–400 ppm) measured in the silicate melt by LA-ICPMS and electron microprobe. We therefore use electron microprobe analyses to quantify the abundance of major elements in the metal.

3. RESULTS

3.1. Metal-silicate partitioning

We can consider metal-silicate partitioning of siderophile elements as a basic reaction that defines the distribution of element M between a metal phase and a silicate melt:

$$M^{metal} + \frac{n}{4}O_2 = MO_{n/2}^{silicate} \quad (1)$$

with n the valence of the cation M in the silicate liquid. We can then define the partition coefficient D_M as the ratio of the molar fraction of M in the metallic phase over $MO_{n/2}$ in the silicate liquid:

$$D_M = \frac{x_M^{metal}}{x_{MO_{n/2}}^{silicate}} \quad (2)$$

The effects of variables pressure (P), temperature (T) and melt composition on metal-silicate partitioning can be isolated by treatment of the results independent of fO_2, by considering that the metal-silicate exchange of cation M is related to the reduction-oxidation of iron (e.g., Wade and Wood, 2005; Corgne et al., 2008):

$$MO_{n/2}^{silicate} + \frac{n}{2}Fe^{metal} = \frac{n}{2}FeO^{silicate} + M^{metal} \quad (3)$$

Taking the logarithm of the equilibrium constant K_{app} results in Eq. (4):

$$\log K_{app} = \log \frac{(x_{FeO}^{silicate})^{\frac{n}{2}} \cdot (x_M^{metal})}{(x_{MO_{n/2}}^{silicate}) \cdot (x_{Fe}^{metal})^{n/2}} + \log \frac{(\gamma_M^{metal})}{(\gamma_{Fe}^{metal})^{n/2}} + \log \frac{(\gamma_{FeO}^{silicate})^{n/2}}{(\gamma_{MO_{n/2}}^{silicate})} \quad (4)$$

where the first term on the right hand side of the equation is defined as the exchange coefficient K_M^D and is directly obtained from experiments, whereas the second and third terms relate to the activity coefficients of $M(O)_{n/2}$ and iron. Eq. (4) shows that the activity of siderophile elements in metallic alloys may be affected by the composition of the alloy. These effects can be addressed by using the epsilon approach or using a multiple linear regression approach (Sections 3.1.1,3.1.2).

3.1.1. The epsilon approach

The epsilon approach is a thermodynamic approach used to correct for the effects of solutes on the activities of other solutes in the metal, using interaction and activity coefficients derived mostly from the steelmaking industry (Wade and Wood, 2005). The elemental activity coefficients in the metallic liquid for each experiment were calculated with the epsilon approach using the metal activity calculator accessible via http://norris.org.au/expet/metalact/ (Wade and Wood, 2005) assuming interaction parameters for carbon-absent experiments. For our calculations, we assume the following valences: 2+ for Ni, Co, Ge, Cr, Mn, 3+ for V, 4 or 5+ for P and 4 or 6+ for W (e.g., Corgne et al., 2008; Wood et al., 2014; Appendix Section A.4). Previous workers also found that W exists dominantly as 6+ in silicate melts under ranges of pressures, temperatures or composition that are broader than those studied here (Cottrell et al., 2009a,b; Wade et al., 2012). For Mo, we use either 4+ (at conditions more reducing than $\Delta IW = -1$) or 6+ (at conditions more oxidizing than $\Delta IW = -1$, with IW the fO_2 of the iron-wüstite buffer) (Righter et al., 2016; Appendix Section A.4) and assuming non-ideal mixing behavior of Fe in metal, where γ_{Fe}^{metal} is calculated using the online metal activity calculator (Wade and Wood, 2005). For additional details of the epsilon approach the reader is referred to Appendix Sections A.3 and A.7.

3.1.2. The multiple linear regression approach

The effects of metal composition on metal-silicate partitioning of siderophile elements can also be studied by performing multiple linear regression on a wide range of compiled experimental metal-silicate partitioning data (e.g., Righter, 2011a; Rai and van Westrenen, 2013, 2014; Steenstra et al., 2016a, 2017a) (Eq. (5)):

$$\log D = a + b(\Delta IW) + c_1(x_{MgO}^{silicate}) + c_2(x_{SiO_2}^{silicate}) + c_3(x_{Al_2O_3}^{silicate}) + c_4(x_{CaO}^{silicate}) + c_5(x_{FeO}^{silicate}) + d(1/T) + e(P/T) + fln(1 - x_S^{metal}) + gln(1 - x_C^{metal}) + hln(1 - x_{Ni}^{metal}) \quad (5)$$

where D is the metal-silicate partition coefficient of an element, defined by its weight concentration in metal divided by its weight concentration in silicate, T is temperature in Kelvin and P is pressure in GPa. Parameter ΔIW is the oxygen fugacity (fO_2) relative to the iron–wüstite buffer (IW), defined by Eq. (6):

$$\Delta IW = 2\log\left(\frac{a_{FeO}^{silicate}}{a_{Fe}^{metal}}\right) = 2\log\left(\frac{x_{FeO}^{silicate}}{x_{Fe}^{metal}}\right) + 2\log\frac{\gamma_{FeO}^{silicate}}{\gamma_{Fe}^{metal}} \quad (6)$$

where $a_{FeO}^{silicate}$ and $x_{FeO}^{silicate}$ are the activity and molar fraction of FeO in the silicate melt and a_{Fe}^{metal} and x_{Fe}^{metal} the activity and molar fraction of Fe in the metal phase, respectively (e.g., Siebert et al., 2011). The effect of silicate melt composition is parameterized using mole oxide fractions of the silicate melt (Eq. (5)) and x_S^{metal}, x_C^{metal} and x_{Ni}^{metal} represent the molar fractions of sulfur, carbon and nickel in the metallic alloy. The latter parameters mimic the Margules parameters for activity coefficients as used in the epsilon approach (Righter, 2011a). Although we do not explicitly take into account the effects of solutes other than S, C, and Ni on siderophile element activities into account, the agreement between the epsilon and multiple linear regression approaches suggests these effects are limited.

The drawbacks and advantages of both parameterization approaches have been discussed elsewhere (e.g. Burkemper et al., 2012; Steenstra et al., 2016b), and the outcome of both approaches is very similar. We use K_{app} values (Eq. (4)) to assess the effect of silicate melt composition, whereas we use the multiple linear regression approach (Eq. (5)) to study core formation in the APB because the latter approach is more convenient.

3.2. Oxygen fugacity and valence states

Oxygen fugacity (fO_2) exerts a major control on the partitioning behavior of siderophile elements, generally resulting in a decrease of D with increasing fO_2, with their slope defining their dominant valence state in the silicate melt

Table 2
Major and minor element composition of silicate melts determined by EPMA and LA–ICP–MS.

Run #	GGS–1	GGS–2	GGS–3	GGS–4	GGS–5	GGS–6	GGS–9	GGS–10	GGS–11	GGS–12	GGS–16	GGS–18
EPMA (wt.%)	*N = 63*[a]	*N = 71*	*N = 54*	*N = 67*	*N = 72*	*N = 15*	*N = 52*	*N = 50*	*N = 54*	*N = 48*	*N = 66*	*N = 46*
MgO	12.76(2.23)[b]	16.71(2.11)	14.33(2.46)	13.58(2.02)	11.39(2.50)	3.80(0.99)	14.83(2.54)	16.92(1.38)	11.76(2.75)	14.82(1.29)	21.81(2.15)	17.84(2.09)
SiO_2	35.23(0.18)	39.06(0.13)	38.02(0.24)	38.50(0.21)	29.73(0.89)	25.77(0.30)	38.18(0.22)	35.51(0.33)	35.05(0.33)	34.45(0.28)	35.46(0.23)	31.55(0.30)
Al_2O_3	8.61(1.06)	8.54(0.83)	9.01(1.02)	7.80(0.82)	7.89(1.17)	9.55(0.49)	10.54(1.18)	7.20(0.40)	8.32(0.85)	7.37(0.39)	7.04(0.71)	7.25(0.43)
CaO	10.12(1.29)	11.08(1.17)	10.47(1.28)	9.09(1.02)	10.09(1.47)	19.71(0.89)	13.45(1.59)	8.97(0.69)	13.70(1.52)	8.69(0.60)	8.29(0.92)	9.71(1.07)
FeO	29.97(0.60)	22.16(0.34)	25.53(0.37)	27.81(0.42)	35.53(0.83)	28.34(0.81)	19.92(0.60)	25.76(0.21)	24.30(0.55)	28.89(0.24)	24.44(0.52)	25.84(0.41)
MnO	0.13(0.01)	0.15(0.01)	0.15(0.01)	0.14(0.01)	0.14(0.01)	0.14(0.01)	0.16(0.01)	0.153(0.004)	0.150(0.005)	0.143(0.003)	0.144(0.005)	0.17(0.01)
Cr_2O_3	0.38(0.01)	0.36(0.01)	0.39(0.01)	0.41(0.01)	0.17(0.08)	n.d.[c]	0.23(0.02)	0.23(0.03)	0.07(0.02)	0.39(0.05)	0.33(0.01)	0.13(0.02)
TiO_2	0.28(0.04)	0.30(0.03)	0.29(0.04)	0.26(0.03)	0.27(0.04)	0.30(0.02)	0.35(0.04)	0.24(0.02)	0.29(0.03)	0.25(0.02)	0.23(0.03)	0.25(0.02)
V_2O_3	–	–	–	–	–	–	–	3.10(0.32)	1.90(0.24)	2.44(0.22)	–	2.78(0.24)
P_2O_5	0.78(0.07)	0.44(0.03)	0.56(0.04)	0.74(0.05)	1.22(0.15)	3.88(0.22)	0.60(0.04)	1.27(0.09)	2.68(0.32)	1.27(0.06)	0.86(0.06)	1.75(0.14)
WO3	0.66(0.09)	0.18(0.03)	n.d.	0.37(0.06)	2.39(0.40)	6.84(0.37)	0.26(0.05)	0.52(0.04)	0.90(0.11)	0.71(0.05)	0.49(0.06)	0.99(0.10)
SO3	0.06(0.01)	0.11(0.01)	0.25(0.03)	0.66(0.08)	0.94(0.16)	1.96(0.29)	0.17(0.02)	0.25(0.02)	0.35(0.04)	0.57(0.04)	0.56(0.07)	0.71(0.08)
Total	99.05(0.23)	99.24(0.24)	99.06(0.22)	99.53(0.16)	99.87(0.30)	100.49(0.51)	99.02(0.20)	100.27(0.12)	99.65(0.19)	100.15(0.13)	99.75(0.13)	99.08(0.21)
LA–ICP–MS	*N = 6*	*N = 8*	*N = 10*	*N = 3*	*N = 7*	*N = 4*	*N = 5*	*N = 5*	*N = 5*	*N = 5*	*N = 8*	*N = 9*
CaO (wt.%)	8.94(0.12)[b]	11.14(0.28)	9.71(0.19)	8.22(0.33)	8.27(0.36)	16.29(1.24)	12.62(0.69)	8.18(0.41)	9.35(0.96)	8.55(0.80)	8.24(0.27)	8.49(0.54)
TiO_2	0.27(0.003)	0.31(0.01)	0.28(0.004)	0.24(0.01)	0.24(0.01)	0.30(0.02)	0.34(0.01)	0.23(0.01)	0.23(0.03)	0.25(0.02)	0.24(0.01)	0.24(0.01)
V_2O_3	–	–	–	–	–	–	–	3.15(0.28)	1.88(0.26)	2.42(0.14)	–	2.85(0.12)
Cr_2O_3	0.37(0.01)	0.37(0.01)	0.41(0.004)	0.38(0.01)	0.30(0.01)	0.08(0.02)	0.32(0.02)	0.23(0.03)	0.09(0.01)	0.36(0.02)	0.33(0.01)	0.16(0.01)
Mn (ppm)	981(10)	1115(11)	1116(7)	1058(22)	968(12)	1105(36)	1078(31)	1110(8)	999(57)	1032(27)	1098(26)	1164(30)
Co	141(3)	91(2)	121(2)	244(7)	177(6)	220(25)	95(4)	137(6)	134(8)	216(9)	161(5)	150(4)
Ni	15(3)	8.0(0.8)	11.0(0.3)	28(1)	14(1)	24(3)	8.1(1.2)	12(1)	13(1)	17(1)	17(2)	11(1)
Ge	–	–	–	–	–	–	–	24(5)	26(2)	35(4)	–	27(3)
Mo	36(1)	13(2)	13(1)	31.5(0.1)	130(11)	792(52)	11(1)	27(3)	25(2)	47(8)	33(2)	37(4)
W	5079(156)	1711(57)	2422(28)	2844(72)	15,062(802)	41,097(2702)	2515(145)	3559(143)	5150(363)	4771(191)	3644(242)	6071(345)

Run #	LGS–4	LGS–5	LGS–7	LGS–11	LGS–12	LGS–13	LGS–14	LGS–15	LGS–16	LGS–17	KB–1	KB–2
EPMA (wt.%)	*N = 48*	*N = 52*	*N = 34*	*N = 30*	*N = 33*	*N = 57*	*N = 42*	*N = 42*	*N = 49*	*N = 49*	*N = 38*	*N = 38*
MgO	9.89(0.06)	9.34(0.04)	9.11(0.11)	22.30(1.17)	21.20(0.38)	20.75(0.50)	24.14(1.33)	23.18(0.15)	20.10(1.36)	19.53(0.81)	24.66(2.97)	29.28 (4.00)
SiO_2	56.54(0.14)	50.63(0.08)	51.27(0.18)	45.54(0.32)	46.69(0.13)	42.18(0.23)	42.73(0.13)	47.01(0.08)	41.57(0.31)	41.94(0.20)	28.18(0.67)	30.07(1.12)
Al_2O_3	11.10(0.04)	9.73(0.03)	9.50(0.06)	8.85(0.38)	11.66(0.10)	9.54(0.13)	10.15(0.38)	10.12(0.06)	8.71(0.38)	8.00(0.20)	6.79(0.30)	6.51(0.70)
CaO	1.42(0.02)	1.26(0.01)	1.58(0.12)	1.04(0.09)	1.97(0.11)	1.43(0.07)	1.38(0.10)	1.31(0.03)	1.65(0.14)	1.39(0.06)	11.32(1.24)	10.38(1.54)
FeO	11.62(0.12)	21.31(0.11)	20.51(0.17)	13.81(0.26)	5.52(0.13)	14.56(0.27)	9.72(0.25)	8.14(0.11)	11.46(0.14)	12.52(0.19)	16.93(0.85)	13.84(1.00)
MnO	0.03(0.01)	0.03(0.01)	0.04(0.01)	0.03(0.01)	0.031(0.004)	0.033(0.03)	1.38(0.04)	0.73(0.01)	3.91(0.07)	4.40(0.08)	0.020(0.004)	0.012(0.004)
Cr_2O_3	–	–	–	–	–	–	1.01(0.05)	0.66(0.01)	1.67(0.14)	1.85(0.12)	–	–
TiO_2	0.31(0.01)	0.28(0.01)	0.25(0.01)	0.24(0.02)	0.31(0.01)	0.26(0.01)	0.26(0.02)	0.263(0.004)	0.23(0.01)	0.21(0.01)	2.72(0.20)	2.54(0.30)
Na_2O	0.70(0.01)	0.58(0.01)	0.55(0.01)	0.31(0.02)	0.68(0.01)	0.31(0.01)	0.57(0.03)	0.52(0.01)	0.65(0.04)	0.59(0.02)	2.37(0.37)	2.29(0.50)
K_2O	8.35(0.05)	6.94(0.04)	7.03(0.08)	5.71(0.23)	7.61(0.06)	5.89(0.09)	6.41(0.27)	6.00(0.05)	6.65(0.04)	6.21(0.18)	1.63(0.23)	1.52(0.30)
V_2O_3	–	–	–	–	0.97(0.02)	1.13(0.03)	1.58(0.06)	0.84(0.01)	2.42(0.15)	2.51(0.13)	1.41(0.19)	0.73(0.07)
P_2O_5	0.17(0.01)	0.31(0.02)	0.24(0.01)	0.11(0.01)	0.017(0.005)	0.21(0.03)	0.25(0.01)	0.13(0.01)	0.08(0.01)	0.091(0.004)	2.60(0.25)	1.90(0.23)
WO3	0.08(0.03)	0.16(0.04)	0.06(0.03)	n.d.	n.d.	n.d.	0.09(0.01)	0.05(0.01)	n.d.	n.d.	1.75(0.25)	1.36(0.26)
SO3	0.15(0.02)	0.33(0.01)	0.27(0.01)	0.28(0.02)	0.19(0.01)	0.34(0.02)	0.70(0.06)	0.51(0.06)	0.028(0.004)	0.023(0.003)	1.11(0.16)	1.61(0.33)

(*continued on next page*)

Table 2 (*continued*)

Total	100.43(0.11)	100.97(0.10)	100.04(0.28)	98.27(0.17)	96.96(0.12)	97.26(0.16)	100.47(0.14)	99.55(0.11)	99.80(0.14)	99.93(0.13)	101.67(0.21)	102.19(0.37)
LA–ICP–MS	*N = 6*	*N = 9*	*N = 7*	*N = 13*	*N = 8*	*N = 9*	*N = 12*	*N = 12*	*N = 12*	*N = 11*	*N = 10*	*N = 11*
CaO (wt.%)	1.31(0.06)	1.18(0.02)	1.31(0.05)	1.03(0.02)	1.80(0.03)	1.30(0.04)	1.28(0.04)	1.23(0.01)	1.53(0.03)	1.21(0.07)	11.26(0.52)	10.93(0.94)
TiO_2	0.30(0.01)	0.28(0.003)	0.29(0.01)	0.25(0.01)	0.32(0.01)	0.26(0.01)	0.27(0.01)	0.27(0.003)	0.24(0.003)	0.20(0.01)	2.76(0.09)	2.63(0.15)
V_2O_3	–	–	–	–	1.03(0.02)	1.17(0.03)	1.55(0.03)	0.79(0.01)	2.45(0.04)	2.32(0.08)	1.54(0.03)	0.93(0.03)
Cr_2O_3	–	–	–	–	–	–	1.00(0.02)	0.61(0.01)	1.58(0.04)	1.58(0.07)	–	–
Mn (ppm)	236(8)	233(2)	263(5)	210(4)	207(4)	208(4)	10,979(240)	5480(71)	30,257(265)	31,209(627)	157(4)	108(5)
Co	48(5)	107(1)	117(2)	86(2)	34(1)	107(2)	96(2)	74.0(0.3)	47(1)	54(2)	121(2)	104(4)
Ni	5.8(1.4)	6.4(0.6)	8.4(1.8)	8.0(0.7)	3.1(0.4)	7.7(0.5)	10.8(0.4)	8.0(0.2)	5.2(0.4)	6.9(1.2)	11(1)	15(2)
Ge	–	–	–	–	3.3(0.5)	16(1)	26(1)	21(2)	3.7(0.3)	5.2(0.4)	52(1)	99(8)
Mo	0.7(0.2)	4.3(0.6)	3.6(0.6)	1.7(0.1)	0.3(0.1)	4.0(0.4)	4.7(0.3)	1.6(0.1)	2.9(0.2)	3.3(0.2)	128(4)	148(10)
W	186(29)	941(101)	2014(203)	374(17)	25(2)	661(31)	584(21)	255(13)	248(6)	267(9)	12,705(415)	10,002(693)

Run #	KB–3	KB–4	KB–5	KB–6	BG–1	BG–2	BG–4
EPMA (wt.%)	*N = 63*	*N = 35*	*N = 45*	*N = 40*	*N = 33*	*N = 25*	*N = 42*
MgO	24.86(2.29)	25.72(2.56)	26.54(2.82)	24.88(1.94)	24.91(2.28)	22.72(2.37)	24.34(1.42)
SiO_2	33.30(0.28)	32.43(0.38)	33.14(0.35)	31.51(0.36)	20.08(0.78)	22.37(0.41)	21.36(0.69)
Al_2O_3	7.94(0.40)	6.41(0.42)	7.61(0.48)	8.16(0.34)	4.00(0.15)	3.16(0.13)	4.11(0.13)
CaO	12.82(1.08)	12.82(1.11)	13.02(1.32)	14.81(0.72)	6.73(1.01)	10.27(1.75)	8.22(0.82)
FeO	8.32(0.25)	10.05(0.40)	6.65(0.31)	6.86(0.25)	26.10(0.94)	18.95(0.45)	22.49(0.49)
MnO	0.61(0.02)	1.65(0.04)	1.46(0.04)	1.00(0.02)	0.22(0.01)	3.61(0.08)	1.19(0.02)
Cr_2O_3	0.80(0.09)	0.55(0.09)	0.72(0.12)	0.32(0.03)	0.47(0.09)	0.74(0.12)	0.51(0.05)
TiO_2	3.35(0.19)	2.92(0.21)	3.19(0.22)	3.82(0.20)	14.92(0.73)	11.75(0.42)	15.89(0.63)
Na_2O	2.81(0.29)	2.87(0.40)	3.14(0.44)	3.50(0.34)	0.20(0.04)	0.57(0.07)	0.26(0.03)
K_2O	1.75(0.15)	2.03(0.22)	2.17(0.25)	2.33(0.19)	0.14(0.02)	0.46(0.14)	0.19(0.02)
V_2O_3	1.30(0.07)	1.25(0.11)	0.93(0.12)	0.66(0.04)	n.d.	0.72(0.18)	n.d
P_2O_5	0.99(0.06)	0.85(0.06)	0.56(0.05)	1.35(0.05)	0.99(0.11)	2.35(0.34)	0.97(0.07)
WO3	0.73(0.02)	0.43(0.05)	0.14(0.01)	0.47(0.04)	1.01(0.16)	1.13(0.22)	0.77(0.08)
SO3	0.93(0.08)	0.05(0.01)	0.07(0.01)	1.74(0.17)	1.33(0.43)	0.10(0.01)	0.13(0.01)
Total	100.62(0.25)	100.14(0.38)	99.41(0.37)	101.51(0.32)	101.28(0.50)	99.02(0.45)	100.52(0.32)
LA–ICP–MS	*N = 13*	*N = 12*	*N = 14*	*N = 12*	*N = 12*	*N = 12*	*N = 10*
CaO (wt.%)	12.11(0.34)	10.53(0.77)	11.81(1.52)	14.14(0.39)	7.24(0.25)	10.55(0.93)	8.47(0.46)
TiO_2	3.28(0.07)	2.57(0.17)	2.90(0.30)	3.72(0.07)	15.67(0.32)	10.47(0.30)	16.41(0.60)
V_2O_3	1.10(0.01)	1.30(0.05)	0.97(0.06)	0.91(0.01)	0.87(0.04)	1.21(0.09)	0.74(0.03)
Cr_2O_3	0.69(0.02)	0.51(0.06)	0.57(0.09)	0.30(0.01)	0.37(0.02)	0.51(0.07)	0.38(0.03)
Mn (ppm)	4782(66)	11,455(276)	10,569(427)	7678(79)	1684(22)	25,270(637)	9121(140)
Co	96(2)	58(2)	30(1)	66(2)	322(5)	92(4)	117(3)
Ni	15(1)	7.8(1.1)	5.5(0.4)	13(1)	56(1)	12(1)	32(2)
Ge	35(1)	17(1)	7.1(0.6)	38(2)	175(5)	29(1)	46(3)
Mo	16(1)	23(2)	6.3(0.4)	24(2)	282(5)	65(2)	92(3)
W	2200(57)	2995(320)	957(122)	3109(71)	7795(309)	7808(752)	5066(279)

[a] Number of analyses.
[b] Values in parentheses are 2 standard errors for EPMA and LA–ICPMS in terms of least digits cited.
[c] Not determined.

Table 3
Major and minor element composition of metallic melts determined by EPMA and LA–ICP–MS.

Run #	GGS–1	GGS–2	GGS–3	GGS–4	GGS–5	GGS–6	GGS–9	GGS–10	GGS–11	GGS–12	GGS–16	GGS–18
EPMA (wt.%)	*N = 67*[a]	*N = 81*	*N = 72*	*N = 68*	*N = 63*	*N = 98*	*N = 64*	*N = 41*	*N = 49*	*N = 64*	*N = 71*	*N = 56*
Fe	90.48(0.21)[b]	91.04(0.37)	89.94(0.39)	82.53(0.38)	87.85(0.52)	87.00(0.20)	87.52(0.40)	83.89(0.35)	83.31(0.26)	80.86(0.39)	84.68(0.52)	83.34(0.47)
P	0.52(0.04)	0.72(0.08)	0.38(0.05)	0.18(0.01)	0.23(0.02)	0.102(0.004)	0.64(0.05)	0.95(0.07)	1.02(0.08)	0.88(0.10)	0.66(0.06)	1.06(0.13)
V	–	–	–	–	–	–	–	0.032(0.004)	0.025(0.004)	0.03(0.01)	–	0.04(0.02)
Cr	0.008(0.002)	0.01(0.01)	0.01(0.01)	0.01(0.01)	b.d.l.	b.d.l.	b.d.l.	0.003(0.001)	0.003(0.001)	0.009(0.004)	0.019(0.003)	0.004(0.004)
Mn	0.008(0.002)	0.009(0.003)	0.011(0.003)	0.010(0.003)	0.009(0.003)	0.010(0.003)	0.010(0.004)	0.004(0.002)	0.003(0.002)	0.003(0.001)	0.002(0.001)	0.003(0.002)
Co	1.89(0.02)	1.63(0.01)	1.73(0.03)	2.61(0.04)	2.20(0.03)	2.87(0.02)	2.53(0.10)	2.18(0.03)	2.37(0.02)	2.75(0.04)	2.08(0.04)	2.14(0.04)
Ni	1.85(0.05)	1.52(0.01)	1.76(0.05)	3.19(0.06)	1.94(0.02)	2.42(0.02)	1.77(0.04)	1.46(0.01)	1.85(0.01)	1.97(0.03)	1.85(0.04)	1.51(0.03)
Ge	–	–	–	–	–	–	–	2.51(0.15)	2.48(0.04)	2.83(0.07)	–	2.24(0.06)
Mo	1.88(0.05)	1.60(0.09)	1.58(0.08)	3.04(0.11)	3.22(0.10)	2.94(0.04)	2.22(0.14)	2.53(0.16)	2.45(0.11)	2.81(0.22)	2.21(0.14)	2.48(0.17)
W	1.46(0.03)	1.40(0.03)	1.44(0.04)	1.65(0.06)	1.31(0.04)	0.45(0.03)	2.00(0.04)	2.32(0.05)	2.29(0.05)	2.12(0.11)	1.67(0.06)	1.92(0.07)
S	0.20(0.07)	0.82(0.27)	0.75(0.30)	2.34(0.31)	1.35(0.45)	2.95(0.22)	1.57(0.32)	1.62(0.38)	1.62(0.25)	3.15(0.64)	4.29(0.68)	4.30(0.85)
Total	98.31(0.14)	98.75(0.13)	97.60(0.15)	95.56(0.19)	98.13(0.19)	96.99(0.20)	98.27(0.11)	97.49(0.09)	97.49(0.09)	97.47(0.07)	97.47(0.10)	99.05(0.23)
LA (ppm)	*N = 10*	*N = 9*	*N = 9*	*N = 5*	*N = 7*	*N = 5*	*N = 10*	*N = 3*	*N = 5*	*N = 8*	*N = 8*	*N = 6*
V	–	–	–	–	–	–	–	576(20)	278(52)	98(10)	–	114(14)
Cr	122(8)[b]	249(17)	280(30)	179(7)	116(4)	62(8)	202(11)	80(17)	52(10)	113(7)	376(15)	70(17)
Mn	3.0(0.3)	5.5(0.9)	5.9(1.3)	b.d.[c]	4.4(0.6)	3.6(0.5)	4.8(0.8)	n.d. [d]	12(2)	4.0(0.5)	11(2)	3.7(0.7)
Co	17,994(366)	15,449(279)	16,912(104)	23,905(523)	20,368(231)	26,858(515)	18,202(236)	17,723(428)	20,782(468)	25,055(795)	17,114(234)	17,298(638)
Ge	–	–	–	–	–	–	–	21,451(7505)	22,995(1321)	28,062(967)	–	20,895(265)
Mo	15,326(398)	11,313(301)	14,915(254)	20,295(969)	25,862(768)	20,763(803)	19,677(972)	20,487(5796)	20,410(1316)	20,427(896)	13,845(474)	18,748(507)
W	9795(220)	8031(200)	10,703(130)	9598(505)	8586(438)	2520(80)	14,319(335)	13,155(2286)	15,626(1268)	12,962(934)	9413(290)	8556(147)

Run #	LGS–4	LGS–5	LGS–7	LGS–11	LGS–12	LGS–13	LGS–14	LGS–15 (FeS)	LGS–15 (S–poor)	LGS–16	LGS–17	KB–1
EPMA (wt.%)	*N = 81*	*N = 104*	*N = 103*	*N = 55*	*N = 56*	*N = 92*	*N = 49*	*N = 29*	*N = 30*	*N = 56*	*N = 56*	*N = 42*
Fe	85.54(0.38)	82.97(0.61)	84.69(0.28)	85.13(0.19)	83.46(0.58)	82.99(0.67)	76.93(0.67)	61.88(1.17)	77.59(0.37)	90.48(0.16)	90.52(0.16)	84.73(0.54)
P	1.75(0.09)	0.92(0.08)	1.47(0.06)	1.06(0.06)	1.31(0.11)	0.96(0.11)	1.76(0.18)	0.08(0.05)	2.36(0.18)	0.87(0.06)	1.13(0.07)	0.36(0.04)
V	–	–	–	–	0.16(0.2)	0.02(0.02)	0.17(0.07)	0.13(0.04)	0.07(0.01)	0.08(0.02)	0.09(0.02)	0.026(0.004)
Cr	–	–	–	–	–	0.020(0.003)		0.37(0.08)	0.11(0.01)	0.23(0.02)	0.25(0.03)	–
Mn	0.007(0.002)	0.008(0.002)	0.007(0.002)	0.003(0.001)	0.003(0.002)	0.003(0.001)	0.02(0.01)	0.36(0.10)	0.004(0.003)	0.02(0.01)	0.03(0.01)	0.003(0.002)
Co	1.85(0.03)	2.39(0.04)	2.02(0.02)	2.16(0.01)	2.29(0.03)	2.27(0.06)	2.39(0.09)	1.00(0.15)	2.58(0.05)	1.74(0.01)	1.65(0.01)	2.31(0.04)
Ni	1.27(0.04)	1.75(0.02)	1.90(0.01)	1.92(0.01)	1.67(0.02)	1.82(0.03)	1.94(0.08)	1.34(0.27)	2.03(0.03)	1.45(0.01)	1.43(0.01)	1.62(0.03)
Ge	–	–	–	–	2.81(0.08)	2.75(0.05)	2.35(0.10)	0.17(0.24)	2.73(0.08)	1.59(0.01)	1.67(0.01)	2.43(0.07)
Mo	1.49(0.08)	3.09(0.15)	2.24(0.06)	3.00(0.08)	3.04(0.13)	3.05(0.15)	2.42(0.17)	0.63(0.12)	2.92(0.16)	1.76(0.05)	1.72(0.05)	2.69(0.13)
W	2.73(0.08)	2.50(0.07)	1.70(0.04)	2.21(0.03)	2.43(0.05)	2.16(0.14)	2.68(0.14)	0.04(0.01)	3.35(0.15)	1.65(0.01)	1.65(0.01)	1.03(0.03)
S	2.97(0.36)	3.83(0.75)	4.12(0.35)	3.96(0.22)	2.61(0.60)	4.77(0.63)	8.30(1.18)	31.63(1.22)	5.82(0.82)	0.22(0.06)	0.15(0.04)	4.72(0.76)
Total	97.72(0.12)	97.55(0.12)	98.22(0.13)	99.46(0.13)	99.80(0.15)	99.23(0.17)	99.31(0.18)	97.67(0.62)	99.58(0.11)	100.10(0.09)	100.32(0.09)	99.92(0.15)

(*continued on next page*)

Table 3 (*continued*)

LA (ppm)	*N = 5*	*N = 10*	*N = 9*	*N = 9*	*N = 7*	*N = 8*	*N = 10*	*N = 10*	*N = 7*	*N = 10*	*N = 10*	*N = 8*
V	–	–	–	–	2044(171)	506(86)	1492(179)	1841(666)	823(89)	1063(256)	947(192)	203(44)
Cr	–	–	–	–	–	–	4355(477)	4554(1106)	1525(204)	2539(308)	2890(324)	–
Mn	b.d.l.	2.8(0.3)	1.9(0.2)	4.8(0.8)	5.2(1.1)	3.3(0.7)	255(33)	481(65)	31(11)	790(313)	438(88)	4.7(1.2)
Co	16,017(870)	20,355(489)	18,460(386)	19,399(170)	20,209(384)	23,997(538)	23,182(552)	8960(664)	19,762(2159)	14,004(206)	14,381(232)	20,030(493)
Ge	–	–	–	–	24,519(1125)	27,408(882)	25,618(1225)	1662(1147)	20,680(2717)	13,787(177)	15,422(365)	21,601(791)
Mo	7977(1189)	23,425(1680)	13,033(685)	13,624(216)	15,850(633)	20,463(1375)	13,859(1108)	3699(584)	20,390(4589)	13,511(283)	12,765(244)	16,729(982)
W	12,768(3602)	16,752(780)	8327(577)	11,173(298)	14,122(686)	15,423(936)	10,548(1135)	405(331)	18,881(4599)	12,037(349)	11,077(244)	5490(198)

Run #	KB–2	KB–3	KB–4	KB–5	KB–6	BG–1	BG–2	BG–4
EPMA (wt.%)	*N = 41*	*N = 54*	*N = 28*	*N = 49*	*N = 39*	*N = 42*	*N = 56*	*N = 42*
Fe	81.62(0.68)	80.36(0.49)	91.15(0.25)	89.94(0.29)	82.61(0.42)	81.77(0.43)	90.15(0.12)	90.29(0.19)
P	0.20(0.03)	0.39(0.03)	0.35(0.03)	0.63(0.09)	0.25(0.01)	0.15(0.02)	0.78(0.05)	0.43(0.05)
V	0.016(0.004)	0.044(0.005)	0.03(0.01)	0.05(0.01)	0.03(0.00)	0.012(0.003)	0.011(0.002)	0.012(0.003)
Cr	–	0.18(0.02)	0.09(0.03)	0.22(0.03)	0.09(0.01)	0.007(0.003)	0.013(0.003)	0.016(0.004)
Mn	0.003(0.002)	0.007(0.002)	0.02(0.01)	0.02(0.01)	0.01(0.01)	0.005(0.002)	0.012(0.004)	0.005(0.003)
Co	2.38(0.06)	2.67(0.06)	1.71(0.01)	1.68(0.01)	2.09(0.03)	2.95(0.06)	1.70(0.01)	1.73(0.01)
Ni	1.73(0.04)	2.17(0.04)	1.47(0.01)	1.44(0.02)	1.57(0.01)	2.01(0.03)	1.44(0.01)	1.57(0.01)
Ge	2.44(0.10)	2.47(0.08)	1.61(0.01)	1.56(0.02)	1.73(0.03)	2.81(0.08)	1.60(0.01)	1.70(0.02)
Mo	2.66(0.14)	2.40(0.15)	1.56(0.04)	1.70(0.10)	1.74(0.05)	3.43(0.23)	1.61(0.04)	1.81(0.07)
W	0.78(0.04)	2.14(0.12)	1.40(0.01)	1.47(0.03)	2.55(0.06)	0.61(0.04)	1.47(0.01)	1.00(0.01)
S	7.46(0.94)	4.67(0.81)	0.14(0.05)	0.31(0.10)	4.35(0.40)	4.66(0.76)	0.16(0.04)	0.32(0.08)
Total	99. 31(0.20)	97.52(0.14)	99.60(0.22)	99.06(0.15)	97.04(0.23)	98.45(0.18)	98.97(0.08)	98.89(0.14)
LA (ppm)	*N = 10*	*N = 10*	*N = 10*	*N = 10*	*N = 10*	*N = 10*	*N = 10*	*N = 10*
V	200(18)	531(70)	223(27)	566(92)	363(57)	31(9)	18(1)	58(9)
Cr	–	2768(270)	919(59)	2606(302)	1090(102)	194(50)	112(9)	277(23)
Mn	4.5(0.8)	130(28)	315(64)	391(59)	255(23)	11(3)	117(5)	113(14)
Co	20,929(308)	22,686(423)	15,317(469)	13,935(1390)	16,594(719)	26,135(1129)	15,040(223)	13,776(116)
Ge	23,122(799)	22,075(558)	14,715(309)	13,771(1331)	18,143(1291)	25,472(685)	14,649(166)	14,277(116)
Mo	15,988(672)	12,950(1020)	11,955(551)	13,858(1291)	10,262(620)	20,844(2454)	13,945(523)	11,810(483)
W	4028(236)	9880(917)	9782(709)	10,883(1007)	11,001(1416)	3421(557)	10,663(515)	5971(141)

[a] Number of analyses.
[b] Values in parentheses are two standard errors in terms of least digits cited.
[c] Below detection limit.
[d] Not determined.

(e.g., Newsom and Drake 1982, 1983; Walter et al., 2000; Righter, 2003; Appendix Section A.4). In Eq. (6), fO_2 is sometimes assumed to reflect ideal behavior of Fe and FeO in which their activity coefficients (γ) are unity. The activity coefficient of FeO in the silicate melt is often assumed to be unity, as a consequence of significant uncertainties in $\gamma_{FeO}^{silicate}$ as a function of silicate melt composition (e.g., O'Neill and Eggins, 2002). In addition, the ratios of $\gamma_{FeO}^{silicate}$ and that of the activity coefficients of siderophile elements in silicate melts have been found to be constant for several elements (O'Neill and Eggins 2002; Siebert et al., 2011). However, γ_{Fe}^{metal} may change with the amount or type of solutes dissolved in the liquid metal. In Table 1, we therefore report both fO_2 assuming ideal mixing behavior of Fe, and that for non-ideal behavior, using the activities of Fe calculated by the online metal activity calculator (Wade and Wood, 2005).

We find that the calculated fO_2 assuming non-ideal behavior is only lower than calculated for the ideal mixing case when significant amounts (several wt.%) of S are dissolved in the metal, because the calculated γ_{Fe}^{metal} is close to 1 for all other experiments (Table 1). In addition, it is likely that γ_{Fe}^{metal} in our non-ideal modeling is overestimated for S-rich Fe alloys (>10 wt.% S; Wood et al., 2014), suggesting that the discrepancy between ideal and non-ideal fO_2 values for runs with S-rich metals is likely smaller than shown in Table 1. Results from this study, summarized in Appendix Section A.4 and assuming non-ideal mixing behavior of Fe, generally confirm the assumed valences of 2+ for Mn, Cr, Ge, Co, Ni, 3+ for V, 5+ for P and 6+ for W. For Mo, we observe a transition from 4+ to 6+ at $\sim\Delta IW = -1$, in excellent agreement with the recent observations of Righter et al. (2016). The inferred 2+ valence for Ge is in excellent agreement with Kegler and Holzheid (2011). However, metal-silicate partitioning data for P, Mo and W from the Knippa basalt (KB) and black glass (BG) series consistently show slopes that are less steep than that from the other compositions considered here (Appendix Section A.4). In these series, we may be observing a 4+ valence state for P, Mo and W. This must result from a change of their solubility, hence activity coefficients, in the silicate melt. Major compositional differences between the KB and BG series and the two other compositions considered are their TiO_2 contents. Our results therefore seem to confirm the findings of O'Neill and Eggins (2002), that suggested enhanced solubility (and therefore decreased activity coefficients) of Mo^{4+} over Mo^{6+} in Ti-rich compositions, relative to Ti-poor compositions. Similar behavior may also be expected for P and W in these compositional series, but more research is needed to confirm these findings. For example, O'Neill et al. (2008) suggest that there is no enhanced solubility of W^{4+} over W^{6+} in Ti-rich silicate melt and that W^{6+} is dominant in silicate melts across a wide fO_2 range. However, the latter study focused on high-SiO_2 compositions, whereas the BG and KB runs contain ~10 wt.% less SiO_2 than the compositions studied by O'Neill et al. (2008). As the trend for all three elements is consistent, we use 4+ valence states for calculation of the K_{app} values of P and W (Eq. (4)) in these two compositional series.

3.3. Silicate melt composition

The use of four silicate melt compositional end-members in our experiments allows us to reassess the effect of silicate melt major element composition on D. By using the epsilon approach (and resulting K_{app} values), the metal-silicate partitioning is corrected for any difference in fO_2 or metallic melt composition (Appendix Sections A.3, A.6). The metal-silicate partitioning of these elements should then only be affected by changes in silicate melt composition. The silicate melt compositions in this study mainly varied in CaO, MgO, FeO and SiO_2 and the new data presented in this study is used to assess their effects on D. The experimental compositional range of Al_2O_3 ($x_{Al_2O_3}^{silicate} = \sim 0.02$–0.07) in this study is too limited to assess its effect.

3.3.1. CaO and MgO

Previous studies have suggested that both CaO and MgO may affect the solubility of some siderophile elements in silicate melts, including Mo and W (O'Neill and Eggins, 2002; O'Neill et al., 2008). Covariance analysis on our new dataset suggests $x_{CaO}^{silicate}$ (and $x_{MgO}^{silicate}$) are not correlated, which makes them independent silicate melt parameters (Appendix Section A.9). We observe a distinct dependency of K_{app} for P, Mo and W on $x_{CaO}^{silicate}$ of the silicate melt (Fig. 2). This can be explained by the formation of silicate melt complexes of the form $CaMO_n$, resulting in a decrease of their metal-silicate partition coefficients (e.g., O'Neill and Eggins, 2002; O'Neill et al. 2008). The effect of CaO seems to be the most dominant factor that determines the metal-silicate partitioning of P, Mo and W as a function of silicate melt composition, which agrees with previous studies that concluded Ca^{2+} has a stronger influence on enhancing the solubilities (and lowering activity coefficients) of both Mo^{4+} and Mo^{6+} and W^{6+}, relative to Mg^{2+} (O'Neill and Eggins, 2002; O'Neill et al. 2008). An increase of $\gamma_{MoO_2}^{silicate}$ with increasing CaO contents of the silicate melt was also reported by Wood and Wade (2013). Given the similar partitioning behavior of P, Mo and W, similar trends are expected for P, which is also evident from our data (Fig. 2). These well-defined trends can be used to correct the K_{app} P, Mo, and W values to study other silicate melt compositional effects (Appendix Section A.7). We note that a strong negative dependency of the metal-silicate partitioning of P, Mo, and W is consistent with the parameterizations proposed by Rai and van Westrenen (2014) and Steenstra et al. (2016a,b). Although the formulation of the parameterizations of Righter et al. (2010) and the datasets used for their parameterizations are slightly different, it is noteworthy to mention that the latter derive a strong increase in D(Mo, P) with CaO contents of the silicate melt – contrary to what is found here. Similarly, Sharp et al. (2015) report a positive CaO term for W using the same type of parameterization, but their negative CaO term for Mo agrees with the work presented here. These differences could be related to which datasets are used for the parameterizations. For example, the parameterizations of Righter et al. (2010) are partly based on the experiments of Jana and Walker (1997b), where the metals contain up to 20

wt.% of trace elements. This most likely will affect the activity of these elements in the metal, which could result in discrepancies. It could also result from correlation between silicate melt parameter terms. In our dataset, we observe no systematic dependency of K_{app} for any of the other elements considered here on $x_{CaO}^{silicate}$.

Similar, but less extreme dependencies of D (P, Mo, W) have been suggested for MgO, which would result from the formation of $MgMO_n$ complexes (O'Neill and Eggins, 2002; O'Neill et al., 2008). This is also what is seen in this study, at least for Mo and P. After correction for variable CaO contents, their K_{app} values clearly decrease with

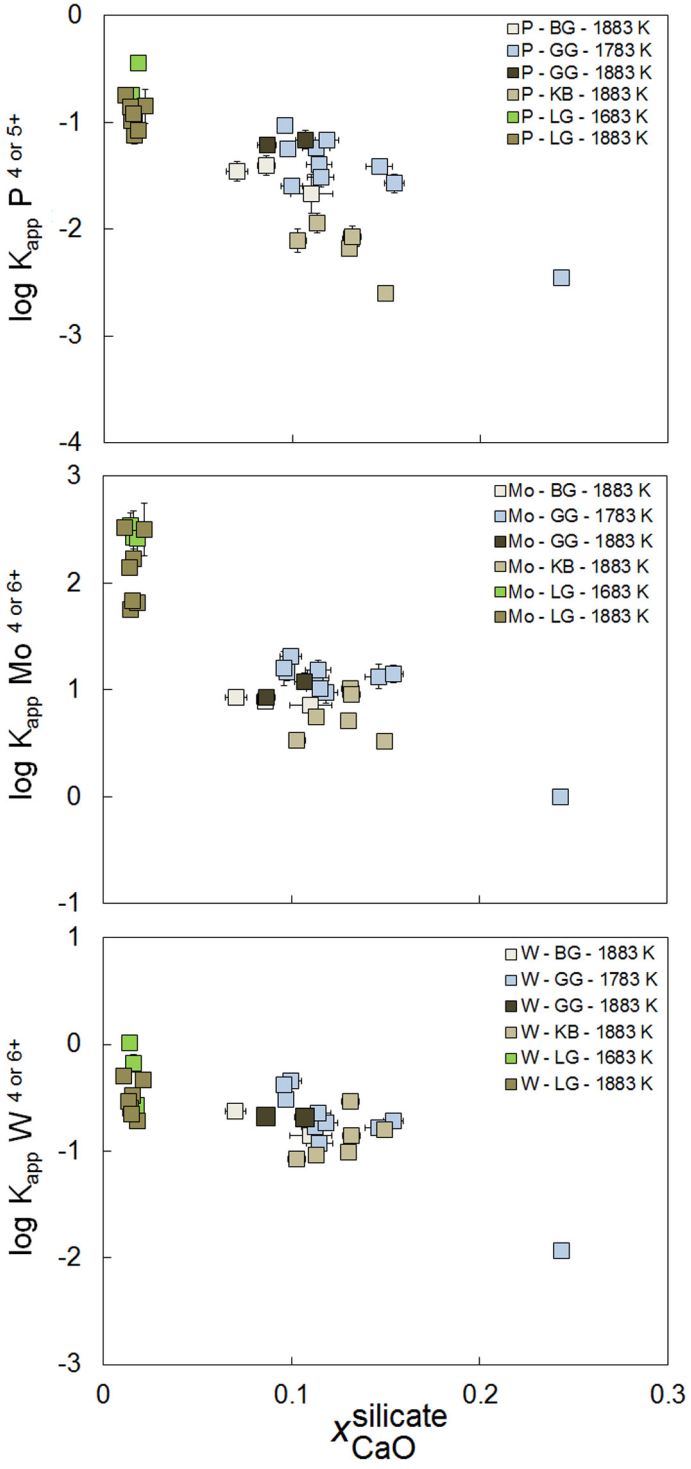

Fig. 2. K_{app} P, Mo, and W versus molar fraction of CaO in the silicate melt (where BG refers to Apollo 14 black glass, GG to Apollo 15 green glass, KB to Knippa basalt and LG to lunar granite). Errors on K_{app} are the maximum errors calculated assuming 2SE for electron microprobe and 2SE for LA-ICPMS analyses and are generally smaller than symbol sizes.

$x_{MgO}^{silicate}$ of the silicate melt (Fig. 3). For Mo, this dependency is somewhat scattered, which is likely due to differences in SiO_2 contents (Fig. 4; see next section). There also seems to be a hint of K_{app} W decreasing with MgO of the silicate melt, although the correlation between K_{app} W and MgO is far less pronounced than that for Mo and P (Fig. 3). The significant offset of the K_{app} W value with the lowest MgO value could result from the unquantified effects of significant amounts of dissolved S in the silicate melts, or alternatively, from an overestimation of the effect of CaO on K_{app} (Appendix Section A.7). The decrease of D(P, Mo, W) with $x_{MgO}^{silicate}$ of the silicate melt is consistent with most previous parameterizations (Rai and van Westrenen, 2014; Sharp et al., 2015; Steenstra et al., 2016a,b; this study). Wood and Wade (2013) reported a decrease of $\gamma_{MoO_2}^{silicate}$ and $\gamma_{WO_3}^{silicate}$ in increasingly more MgO-rich silicate melts. However, Wood and Wade (2013) noted that there are relative high uncertainties in $\gamma_{FeO}^{silicate}$ and in the melting point and entropy of melting of MoO_2, which may explain some of the contradictory observations.

Interestingly, there seems to be some dependency of D(Ni) on the MgO contents of the silicate melt, which will be discussed in more detail in Section 4.1.

3.3.2. SiO_2

The effects of SiO_2 on the metal-silicate partitioning of siderophile elements may be significant due to silicon's network forming capabilities (e.g., Mysen et al., 1982). For a number of elements, no significantly effects of SiO_2 are observed within our new experimental dataset. Exceptions seem to be Ge, V, Ni, and Mo. Their K_{app} values seem to increase with $x_{SiO_2}^{silicate}$ (Fig. 4). These results may imply that polymerization of the silicate melt makes Ge, V, Ni, and Mo less compatible in the silicate melt.

We note that a (non-linear) dependency of $\gamma_{NiO}^{silicate}$ on $x_{SiO_2}^{silicate}$ was also found for Ni by Borisov (2007) (discussed in more detail in Section 4.1). For Ge and Mo, our results agree well with the positive dependencies derived from parameterizations of a wider range of metal-silicate partitioning (Rai and van Westrenen, 2014; Sharp et al., 2015; Steenstra et al., 2016a, this study) and solubility data for Mo^{4+} and Mo^{6+} (Burkemper et al., 2012). Wood and Wade (2013) also suggested that K_D Mo increases with increasing Si contents of the silicate melt. We note that $x_{SiO_2}^{silicate}$ is strongly correlated with both $x_{CaO}^{silicate}$ and $x_{MgO}^{silicate}$ within our new dataset and this likely explains the higher degree of scatter for K_{app} Mo (Appendix Section A.9; Fig. 4). The dependence of D(Ge) on $x_{SiO_2}^{silicate}$ is in agreement with the results of Kegler and Holzheid (2011), who reported a negative dependency of D(Ge) on *nbo/t* of the silicate melt.

Detailed studies on the solubility and activity of V^{3+} are, to our knowledge, not available, which prohibits in depth comparison of our work. Previously reported effects of sta-

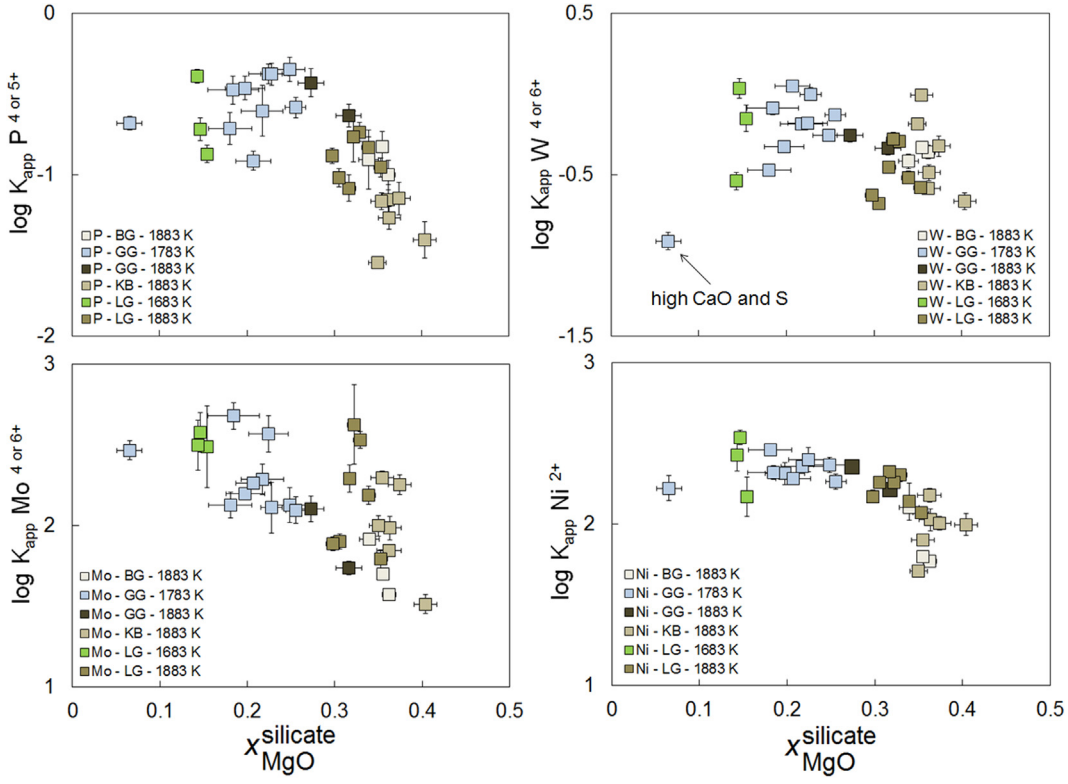

Fig. 3. K_{app} versus molar fraction of MgO ($x_{MgO}^{silicate}$) in the silicate melt. K_{app} P, Mo, W were normalized to $x_{CaO}^{silicate} = 0.01$ (Appendix Section A.7). Errors on K_{app} are the maximum errors calculated assuming 2SE for electron microprobe and 2SE for LA-ICPMS analyses and are generally smaller than symbol sizes.

tistically significant *nbo/t* terms derived for V are at least consistent with our hypothesis that D(V) is dependent on the SiO_2 content of the silicate melt, and therefore, the extent of polymerization of the melt (Wood et al., 2008; Siebert et al., 2011). The dependence of both Ge and V partitioning on $x_{SiO_2}^{silicate}$ could also result from different Al_2O_3 contents as $x_{SiO_2}^{silicate}$ and $x_{Al_2O_3}^{silicate}$ are also highly correlated. However, the range of $x_{Al_2O_3}^{silicate}$ in our dataset is quite limited (0.02–0.07), relative to the $x_{SiO_2}^{silicate}$ range of 0.20–0.50, which implies either that effects of $x_{Al_2O_3}^{silicate}$ are very strong or that $x_{SiO_2}^{silicate}$ indeed affects K_{app} V and Ge.

3.3.3. FeO

Fe^{2+} has been shown to mainly act as a network modifier in silicate melts, thereby affecting the structure of silicate melts (e.g., Mysen and Virgo, 1985) and possibly affecting D. Because the oxidation state of a planetary body during core formation determines the FeO content of the silicate mantle, a wide range of mantle FeO contents are found among the terrestrial bodies. For example, current estimates of FeO in the Martian and lunar mantle are 18 ± 2 wt.% and 10.5 ± 2.5 wt.%, respectively (Rai and van Westrenen 2013, 2014 and references therein). Any effects of FeO on D should therefore be well quantified. After correction of solute interaction in the metal and variable fO_2, it seems however that the metal-silicate partitioning of most siderophile elements considered here is independent of FeO, or only very slightly affected by FeO. This could also be a result of scattering due to the strong positive correlation between $x_{FeO}^{silicate}$ and $x_{CaO}^{silicate}$ and the negative correlation of $x_{FeO}^{silicate}$ with $x_{MgO}^{silicate}$, both of which greatly affect the metal-silicate partitioning of many siderophile element considered here (Appendix Section A.9). An exception is S. Its metal-silicate partitioning has been shown to be independent of fO_2 and fS_2, but instead dependent on silicate melt composition, through FeO and the sulfide capacity or C_S (e.g., Mavrogenes and O'Neill, 1999; Rose-Weston et al., 2009; Boujibar et al. 2014; Steenstra et al. 2016c). Our data are consistent with prior observations: D(S) decreases within the range of relatively high FeO contents of the silicate melts in this work (Fig. 5). At lower FeO, D(S) would decrease as well, resulting in a parabolic dependency of D (S) on the FeO content of the silicate melt (Boujibar et al., 2014). However, the D(S) data for the KB series show a significant offset from the data for the other three compositions. This is likely explained by a silicate melt compositional effect on C_S, which could be related to the different Na_2O and/or possibly K_2O contents of these experiments (Boujibar et al. 2014). We also note that the previously reported strong or negative $x_{FeO}^{silicate}$ dependencies for D(P, Mo, W) (Righter et al., 2010; Rai and van Westrenen 2014; Sharp et al. 2015) are not evident from our new data.

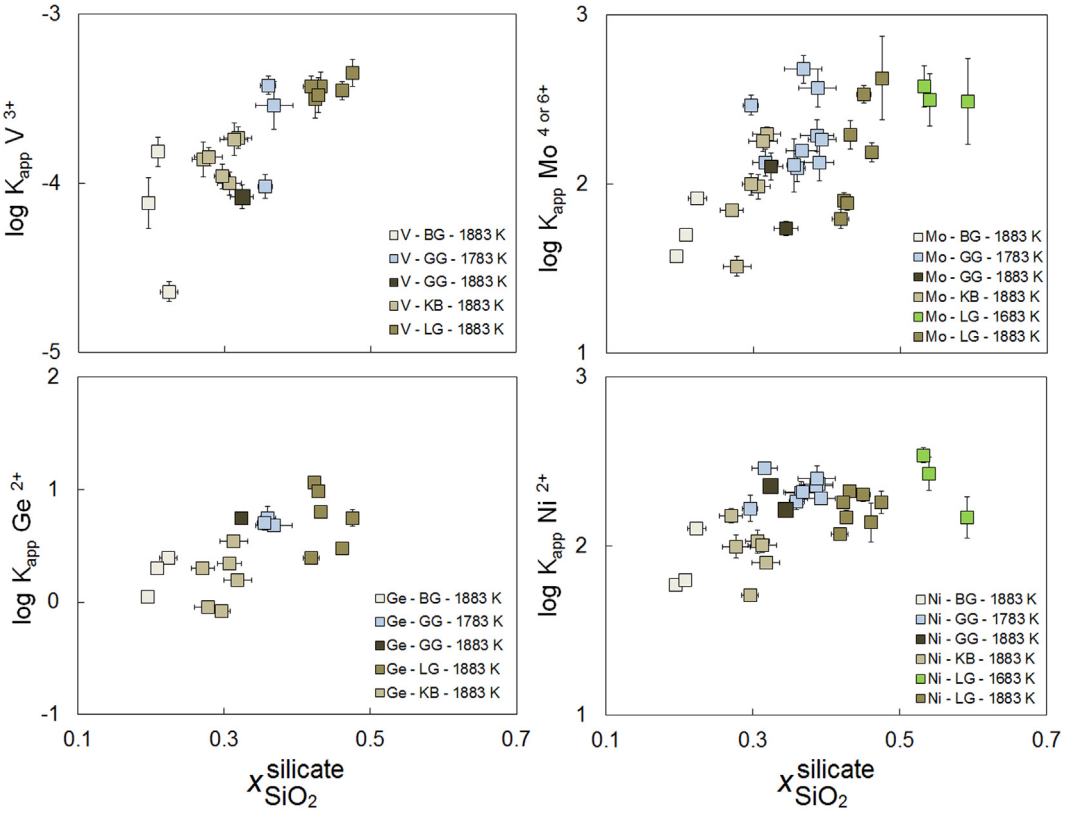

Fig. 4. K_{app} versus molar fraction of SiO_2 ($x_{SiO_2}^{silicate}$) in the silicate melt. K_{app} Mo was normalized to $x_{CaO}^{silicate} = 0.01$ (Appendix Section A.7). Error bars for K_{app} represent the maximum errors assuming 2SE for electron microprobe and 2SE for LA-ICPMS.

4. DISCUSSION

4.1. Effects of silicate melt composition on metal-silicate partitioning of Ni

It is commonly assumed that the metal-silicate partitioning of lower valence elements, including Ni, Co, V, Ge, Mn, and Cr, is not significantly affected by changes in silicate melt composition (Holzheid et al., 1997; Wood et al., 2008; Palme et al., 2011; Siebert et al., 2011). For some elements (Mn, Cr, Co), this assumption is validated by data from this study (Table 4). However, for Ni (and Ge, V), a clear dependence of their metal-silicate partition coefficients on silicate melt composition is observed (Fig. 4; Table 4).

Our data suggests that K_{app} Ni seems to differ with different type of silicate melt compositions considered. Numerous previous workers that studied the distribution of Ni between olivine and silicate melt concluded that MgO is indeed strongly positively correlated with $\gamma_{NiO}^{silicate}$, and thus with NiO solubility in silicate melts (Hart and Davis, 1978; Takahashi, 1978; Campbell et al., 1979; Jones, 1984; Seifert et al., 1988; Ehlers et al., 1992). This would result in decreasing siderophile behavior of Ni with increasing MgO content of the silicate melt. O'Neill and Eggins (2002) also concluded that a fundamental chemical property of melts controls $\gamma_{NiO}^{silicate}$. They also found that there is no obvious correlation between $\gamma_{NiO}^{silicate}$ and any simple compositional variable. Instead, they suggested that $\gamma_{NiO}^{sil\ melt}$ may correlate with $\gamma_{MgO}^{silicate}$, but lack of sufficiently accurate thermodynamic measurements of $\gamma_{MgO}^{silicate}$ prohibits an adequate assessment as of yet (O'Neill and Eggins, 2002). O'Neill and Eggins (2002) predicted that $\gamma_{NiO}^{silicate}$ should initially decrease with MgO until $x_{MgO}^{silicate}$ ~0.16 and then increase again (which would result in an initial increase of K_{app} Ni and subsequent decrease, similar to the observations in this study). Colson et al. (2005) re-examined this issue and developed a predictive model for $\gamma_{NiO}^{silicate}$. They proposed that variations in $\gamma_{NiO}^{silicate}$ are correlated with both the structure of the silicate melt and the MgO and CaO contents of the silicate melt, at least within the range of 0.3–0.55 for $x_{MgO}^{silicate} + x_{CaO}^{silicate}$. Borisov (2006) subsequently studied $\gamma_{NiO}^{silicate}$ in high SiO_2 silicate melts and found that $\gamma_{NiO}^{silicate}$, and hence its solubility, is actually affected by the SiO_2 contents of the silicate melt in a non-linear fashion.

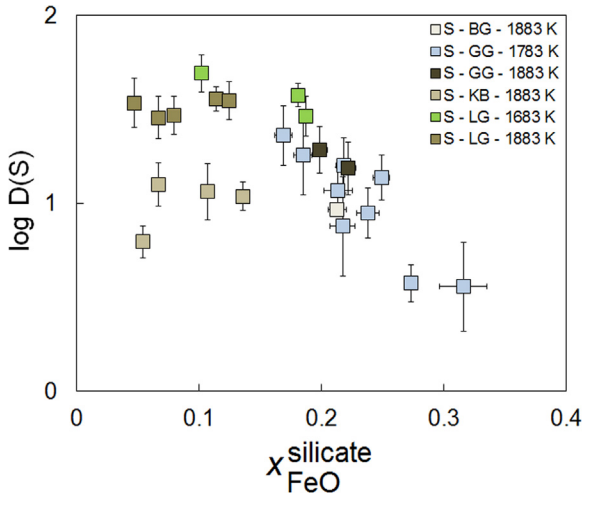

Fig. 5. D (S) versus molar fraction of FeO ($x_{FeO}^{silicate}$) in the silicate melt. Vertical error bars for are propagated from the 2SE errors of repeat analyses of metal and silicate in each run. Horizontal errors represent maximum errors based on 2SE errors of repeat analyses of silicate in each run.

Although the *nbo/t* term (Mysen et al., 1982) has been shown to be insufficient as a single silicate melt compositional term due to contrasting effects of Mg and Ca on activities of trace elements (O'Neill and Eggins, 2002), D (Ni) has been shown to decrease with *nbo/t* from a wider range of studies (e.g., Righter et al., 2011 and references therein). However, Wood and Wade (2013) suggested that $\gamma_{NiO}^{silicate}$ decreases when melts becoming increasingly more forsteritic, which can be considered as an increase of D (Ni) with *nbo/t*. Other workers (e.g., Holzheid et al., 1997; Palme et al. 2011) disputed a compositional dependence of D(Ni), as it was found that $\gamma_{FeO}^{silicate}$ is usually highly correlated with $\gamma_{NiO}^{silicate}$ (O'Neill and Eggins, 2002). Although the activity coefficients are indeed highly correlated, the ratio of $\gamma_{NiO}^{silicate}$ and $\gamma_{FeO}^{silicate}$ has been shown not to be constant (Pretorius and Muan, 1992; O'Neill and Eggins, 2002). This seems to falsify the hypothesis that Ni metal-silicate partitioning is *completely* independent of silicate melt composition as suggested by some workers (e.g., Holzheid et al., 1997; Siebert et al., 2011; Palme et al., 2011), in agreement with the work presented here. Our results are most consistent with the observations of Colson et al. (2005) and Borisov (2006), that suggest that MgO, CaO and SiO_2 affects the solubility of Ni^{2+} in silicate melts. As of yet, these complexities are still not well understood and are difficult to account for in current geochemical models of core formation. Fortunately, the inferred silicate melt compositional dependencies of D(Ni) are limited and will not significantly affect the outcome of geochemical models of core formation.

4.2. Modeling approach used for studying core formation in the angrite parent body

To assess the *X-fO₂* conditions of core formation in the angrite parent body (APB), we combine the new data from this study with previously published experimentally determined metal-silicate and sulfide-silicate partitioning data (Peach and Mathez, 1993; Thibault and Walter, 1995; Gaetani and Grove, 1997; Righter and Drake, 2000; Chabot and Agee, 2003; Kegler et al., 2008; Righter et al., 2010, 2011; Siebert et al., 2011; Wade et al., 2012; Ballhaus et al., 2013; Kiseeva and Wood, 2013; Mungall and Brenan, 2014; Wood et al., 2014; Blanchard et al., 2015; Steenstra et al., 2016c; Supplementary Table 1) in parameterizations using Eq. (5) (Table 4). For some of the elements (P, Co, Ni, Mn, V, Ga) the fO_2 term in Eq. (5) was fixed as it has been shown that these valences are dominant across the fO_2 range relevant for planetary differentiation (Table 4; Appendix Section A.4). The fO_2 value of

Table 4
Parameterizations using new data from this study and compiled metal–silicate partitioning data (see main text). Only statistical valid (≤0.05) variables were considered. Regressions for Co, Ni, Cr, Mn, and V were performed including or excluding (the latter indicated with *) silicate melt compositional parameters. Regressions in bold were used for modeling core formation in the angrite parent body. Uncertainty (1SE) on regression coefficients is given in parentheses.

	a	*b* (ΔIW)	*c1* ($x_{MgO}^{silicate}$)	*c2* ($x_{SiO_2}^{silicate}$)	*c3* ($x_{Al_2O_3}^{silicate}$)	*c4* ($x_{CaO}^{silicate}$)	*c5* ($x_{FeO}^{silicate}$)	*d* (1/*T*)	*e* (*P*/*T*)	$fln\,(1-x_S^{metal})$	$gln\,(1-x_C^{metal})$	$hln\,(1-x_{Ni}^{metal})$	R^2	N^a
P	1.75(72)	−1.25[b]	−2.81(76)		22.54(442)	−10.22(95)	2.71(101)	−6068(1011)	469(118)	4.18(52)			0.82	83
Co	2.52(35)	−0.50[b]	−2.09(32)	−1.20(32)	−1.51(50)	−1.93(36)	−1.78(33)	1210(250)	−79(17)	1.82(06)		0.90(8)	0.92	164
Co*	**0.19(17)**	**−0.50**[b]						**2585(295)**	**−52(21)**	**1.88(07)**	**−0.33(13)**	**1.01(8)**	**0.86**	**164**
Ni	0.35(15)	−0.50[b]		1.27(16)			1.20(18)	2650(293)	−153(24)	1.35(06)			0.82	214
Ni*	**0.38(17)**	**−0.50**[b]						**3748(300)**	**−164(28)**	**1.41(06)**			**0.76**	**214**
Cr	−0.09(20)	−0.41(03)		1.08(20)				−3231(360)		−1.17(10)	−1.34(19)	1.29(47)	0.86	166
Cr*	−0.32(27)	−0.48(03)						−2570(442)	121(51)	−1.15(10)	−1.74(20)		0.86	166
Mn	−0.68(37)	−0.50[b]	−1.88(37)	−3.17(61)		−3.87(74)				−2.12(16)	−2.49(32)		0.56	164
Mn*	−2.73(05)	−0.50[b]								−1.60(14)	−2.06(33)		0.45	164
V	−5.02(35)	−0.75[b]	2.04(37)	2.67(46)	6.08(61)	2.86(68)				−0.82(14)	−4.13(19)		0.91	94
V*	−1.17(51)	−0.75[b]						−3164(879)	261(112)	−0.72(24)	−3.05(33)	2.98(146)	0.71	94
Ga	**2.52(47)**	**−0.75**[b]	**−1.95(28)**			**−4.38(55)**		**−3010(708)**		**3.35(15)**	**2.23(23)**	**−3.68(92)**	**0.94**	**66**
Ge	−1.47(74)	−0.69(14)		3.56(59)		−2.93(81)	4.48(148)	3346(1396)		4.26(27)	2.11(52)		0.88	69
Mo	**−0.31(62)**	**−0.86(09)**	**−1.22(63)**	**3.79(70)**	**7.39(189)**	**−4.50(84)**		**1936(730)**		**1.26(31)**	**−2.51(30)**		**0.89**	**113**
W	**−0.07(26)**	**−1.41(10)**	**−3.81(50)**		**12.40(313)**	**−8.40(80)**		**−592(218)**	**334(104)**	**2.24(51)**	**−4.19(33)**	**−7.83(186)**	**0.83**	**124**

[a] *N* is the number of experimental D values used for regression.
[b] The fO_2 coefficient was fixed assuming a 2+ valence for Co, Ni, Mn; 3+ for V, Ga and 5+ for P.

each experiment in our database was calculated considering the effects of solutes in the metal on γ_{Fe}^{metal}, using the online metal activity calculator (Wade and Wood, 2005). This approach was also used to derive the metal C contents for C-saturated experiments from previous studies.

The possibility of non-linear pressure dependencies on metal-silicate partitioning of siderophile elements is a topic of heated debate (e.g., Kegler et al., 2008; Sanloup et al., 2011; Rai and van Westrenen, 2014; Steenstra et al., 2017b). It has been found that significant structural transitions in Fe-rich alloys occur at ~5.2 GPa (Sanloup et al., 2011). In past studies, some workers therefore parameterized low-pressure (<5 GPa) and high pressure (>5 GPa) metal-silicate partitioning data independently (e.g., Rai and van Westrenen, 2013, 2014). Although parameterizations based on low pressure data and those including both low and high pressure data yield comparable modeling outcomes for Vesta, the Moon and Mars (Righter et al., 1997; Rai and van Westrenen, 2013, 2014; Righter et al., 2015; Steenstra et al., 2016a,b), we only use <5 GPa data here so that our results are independent of the outcome of this debate. Although the exact size of the APB is not well constrained, it is unlikely that pressures at the core-mantle boundary exceeded 5 GPa. For example, the corona and symplectite textures observed in angrite NWA 2999 are not consistent with metamorphic reactions in a large sized planetary body, but instead with cooling upon crystallization of an angritic melt (Hutson et al., 2007). The early crystallization ages for angrites (~4.56 Ga) also argue for a small parent body, as accretion, differentiation and cooling must then have occurred shortly (< several million years) after CAI formation (Schiller et al., 2010; Keil, 2012; Pringle et al., 2014).

Regressions were performed with the SPSS 20 software package and only statistically significant solutions were considered ($p < 0.05$). Individual uncertainties on D values or uncertainties on other terms were not taken into account. Experiments in which the metal contained significant (>0.5 wt.%) amounts of Si were excluded, because Si is unlikely to be present in significant amounts in the APB core. This is suggested from the FeO content of angrites, which implies relatively oxidizing conditions during core formation (e.g., Jurewicz et al., 1993; McKay et al., 1994; Righter, 2008; Shirai et al., 2009). We show in Appendix Section A.8 that the measured metal-silicate partition coefficients from this study and the literature match well with those predicted by the parameterizations listed in Table 4. Data from recently reported independent datasets (Putter et al., 2017; Seegers et al., 2017) are also reproduced well. In addition, the trends of D with silicate and metallic composition observed within the new dataset presented here also in general agree well. For example, the parameterizations listed in Table 4 predict a sharp decrease of the siderophile behavior of P, Mo, and W versus CaO of the silicate melt, which is also clearly seen from our new data set only. Similarly, the inferred valences of Mo (4+) and W (6+) are well reproduced within the new parameterizations. The ln $(1-x_S^{metal})$ terms also agree well with the chalcophile or chalcophobic dependencies derived using the epsilon approach (Appendix Section A.6, A.8; Table 4). However,

it must be acknowledged that the majority of the parameters considered here correlate significantly (Appendix Section A.9). This could also explain some of the contradictory silicate melt dependencies that were previously discussed.

As previously discussed in Section 4.1 above, it is still unclear exactly how silicate melt composition affects D(Co), similar to D(Ni) (O'Neill and Eggins, 2002). It is therefore difficult to assess the reliability of these parameterizations. We do note that the parameterization for Co is based on a wide range of metal-silicate partitioning data and the D values seem to be predicted quite well (Appendix Section A.8). However, it seems that at least for Ni and Co, parameterization of existing data without separate silicate melt compositional terms also results in relatively good fits. Given the limited silicate melt dependencies on the metal-silicate partition coefficients of Ni and Co, we use no silicate melt compositional terms in the parameterizations of Ni and Co. The final set of parameterizations used in our application to core formation in the APB in marked in bold in Table 4.

4.3. Bulk composition and core mass of the angrite parent body

Jurewicz et al. (1993, 2004) suggested from partial melting experiments of Allende CV-chondrite type compositions that the bulk compositions of angrites are most compatible with a volatile depleted and relatively oxidized CV bulk composition. Simple mass balance considerations can then be used to infer the range of FeO and MgO contents of the APB mantle, as well as the plausible range of core masses that are compatible with a CV bulk composition (Appendix Section A.10, Fig. 6). The size and composition of the APB core will affect the FeO contents of the APB mantle and determines the fO_2 (Appendix Section A.10). Independent fO_2 estimates can therefore be used to additionally constrain the APB core mass. Pyroxene cores in Angra dos Reis (King et al., 2012) and olivine cores in LEW 87,051 and Sahara 99,555 (Shearer et al., 2016) suggest $\Delta IW = -0.7 \pm 0.6$, implying a mildly reduced APB interior.

If the APB core is assumed to be made of 100 wt.% pure Fe, no core is formed at conditions more oxidizing than $\Delta IW \sim -1$ (the FeO content of the APB mantle exceeds the total available Fe for a CV bulk composition in that case) (Fig. 6b). This is reduced to $\Delta IW \sim -0.6$ for a 70 wt.% Fe core with 20 wt.% Ni and 10 wt.% S, which is a reasonable upper limit given the Fe content of the lunar core (Rai and van Westrenen, 2014; Steenstra et al., 2016a, 2017a) and vestan core (Steenstra et al., 2016b). Carbon is also a likely constituent of the APB core as about ~0.6 wt.% C is expected for the bulk APB if a CV composition is considered (Newsom, 1995). Although S increases the activity of Fe in the example above, C lowers the activity of Fe resulting in a higher fO_2 upper limit as defined by Eq. (7) (see Appendix Section A.10). This is illustrated by consideration of a hypothetical APB core that contains 20 wt.% Ni, 5 wt.% S and 5 wt.% C, which results in a fO_2 of $\Delta IW < -0.2$ during differentiation of the APB

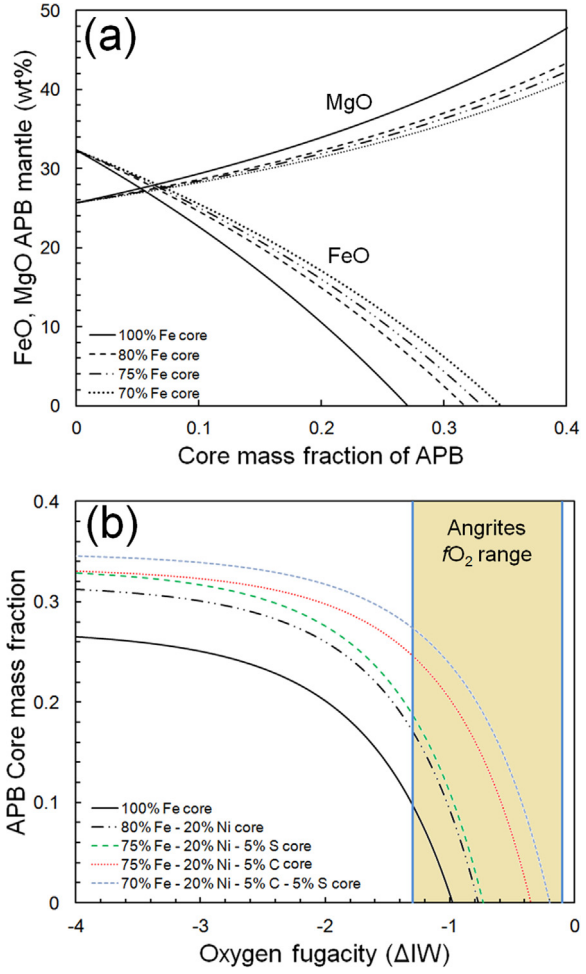

Fig. 6. Angrite parent body compositional calculations assuming a CV bulk composition and non-ideal mixing behavior of Fe. (a) FeO and MgO of the APB mantle for different core compositions as a function of core mass fraction. (b) APB core mass fraction versus fO_2 (ΔIW) for different core compositions.

(Fig. 6b). Therefore, the overall fO_2 during core formation in the APB is constrained to $\Delta IW < -0.2$, depending on core composition (Appendix Section A.10).

We use the APB mantle compositional estimates of Shirai et al. (2009) and assume a CV bulk composition (Appendix Section A.10; Table 5) to assess the siderophile element depletions in the APB. We only consider the siderophile elements depletions of Co, Ni, Ga, Mo, and W, as the APB mantle depletions of the other siderophile elements considered in this study are not known. The metal-silicate partition coefficients that are required to explain their depletion in the APB mantle (D(c/m)) can be calculated by using the following mass balance approach if a certain core composition and mass is assumed (e.g., Rai and van Westrenen, 2013, 2014; Steenstra et al., 2016a,b, 2017a):

$$D_{\frac{c}{m}(i)} = \left(C_{bAPB(i)} - xC_{bsAPB(i)}\right) / \left(C_{bsAPB(i)}(1-x)\right) \quad (7)$$

where CbAPB(i) is the concentration by weight of element *i* in the bulk APB assuming a CV bulk composition (taken from Newsom, 1995), CbsAPB(i) is the estimated abun-

Table 5
Concentrations of major and siderophile elements in the APB (assuming a CV bulk composition). The major element composition of the APB mantle is a function of fO_2 during core formation and varies for each modeling scenario (Appendix Section A.10).

	Bulk APB[a]	Correlations[b]	Bulk silicate APB
MgO (wt.%)	25.7		var.
SiO_2	35.7		
Al_2O_3	3.5		
CaO	2.5		
FeO	32.3		
Co (ppm)	655	Co/Fe	33–56
Ni	11,340	Ni/Mg	68–266
Ga	6	Ga/Al	0.08–0.14
Mo (ppb)	2100	Mo/Nd	15–42
W	190	W/La	11–13

[a] Newsom (1995).
[b] Shirai et al. (2009).

dance of element i in the bulk silicate APB (Shirai et al., 2009; Table 5) and x is the assumed mass fraction of the silicate portion of the APB. We re-calculate the required metal-silicate partition coefficients for each core composition (and therefore core mass) and fO_2 condition that we model (Appendix Section A.10). Examples of calculated D (c/m) values for a pure Fe and a 75 wt.% Fe – 20 wt.% Ni – 5 wt.% C APB core are shown in Fig. 7. In our models we further assume that the temperatures of metal-silicate equilibration at a given pressure are considered to lie between the APB mantle solidus and liquidus. The APB mantle solidus was defined as T_{sol} (K) = 60 * P (GPa) + 1423 and the APB mantle liquidus as T_{liq} (K) = 50 * P (GPa) + 1773 based on the Allende CV3 phase relationships reported by Agee et al. (1995). Although these relationships are based on the composition of the APB prior to core extraction during differentiation, it is unlikely that consideration of higher liquidus temperatures due to lower FeO contents of the APB mantle will change the outcome of this study, as fO_2 is the most dominant variable in these models (see Section 4.4).

We then use a Monte Carlo approach to assess at which compositional and redox conditions the siderophile element partition coefficients match their estimated depletions in the APB mantle (e.g., Rai and van Westrenen, 2013, 2014; Steenstra et al., 2016a,b, 2017a). We perform 10,000 iterations where in each instance D is calculated using Eq. (5) with each set of regression coefficients reported in Table 5. Within the 10,000 iterations, the P-T-X conditions and 1SE errors on the regression coefficients were randomly varied within their defined ranges. If the calculated D is within error of the required D, it is returned as a solution. These solutions thus define a P-T-X-fO_2 solution space, where the predicted metal-silicate partitioning behavior of the siderophile elements considered matches their observed abundances in the APB mantle.

4.4. Core formation in the angrite parent body

We first assess if the observed siderophile element depletions in the APB mantle can be reconciled by equilibration with a pure Fe core at low pressure (0.1 GPa), corresponding to a core-mantle boundary depth of a body of the approximate size of Vesta. Although a pure Fe core is not realistic for planets, we use it to assess the effects of different solutes in the core on the inferred redox state of APB core formation. We observe that the APB mantle depletions of W cannot be explained by metal-silicate equilibration with a pure Fe core, independent of fO_2, as W behaves insufficiently siderophile (Fig. 8a). At conditions more oxidizing than ΔIW = −1.45, there are also no solutions for Ga. At conditions more reducing than ΔIW = −1.55, there are no more solutions for Co and the number of solutions for Ni drastically decreases.

The addition of Ni greatly affects these models. An increase of Ni in the APB core results in a decrease of the

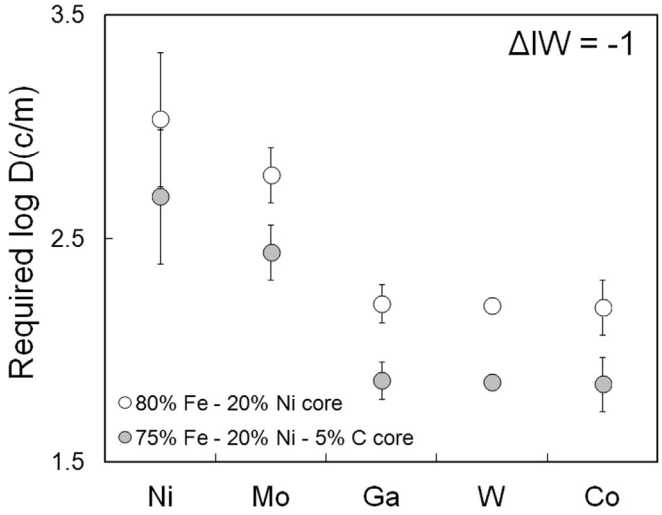

Fig. 7. Examples of D(c/m) values required to explain their depletions in the APB mantle at ΔIW = −1 for a 100 wt.% Fe and a 75 wt.% Fe – 20 wt.% Ni – 5 wt.% C APB core (Shirai et al., 2009). Error bars represent 1SE.

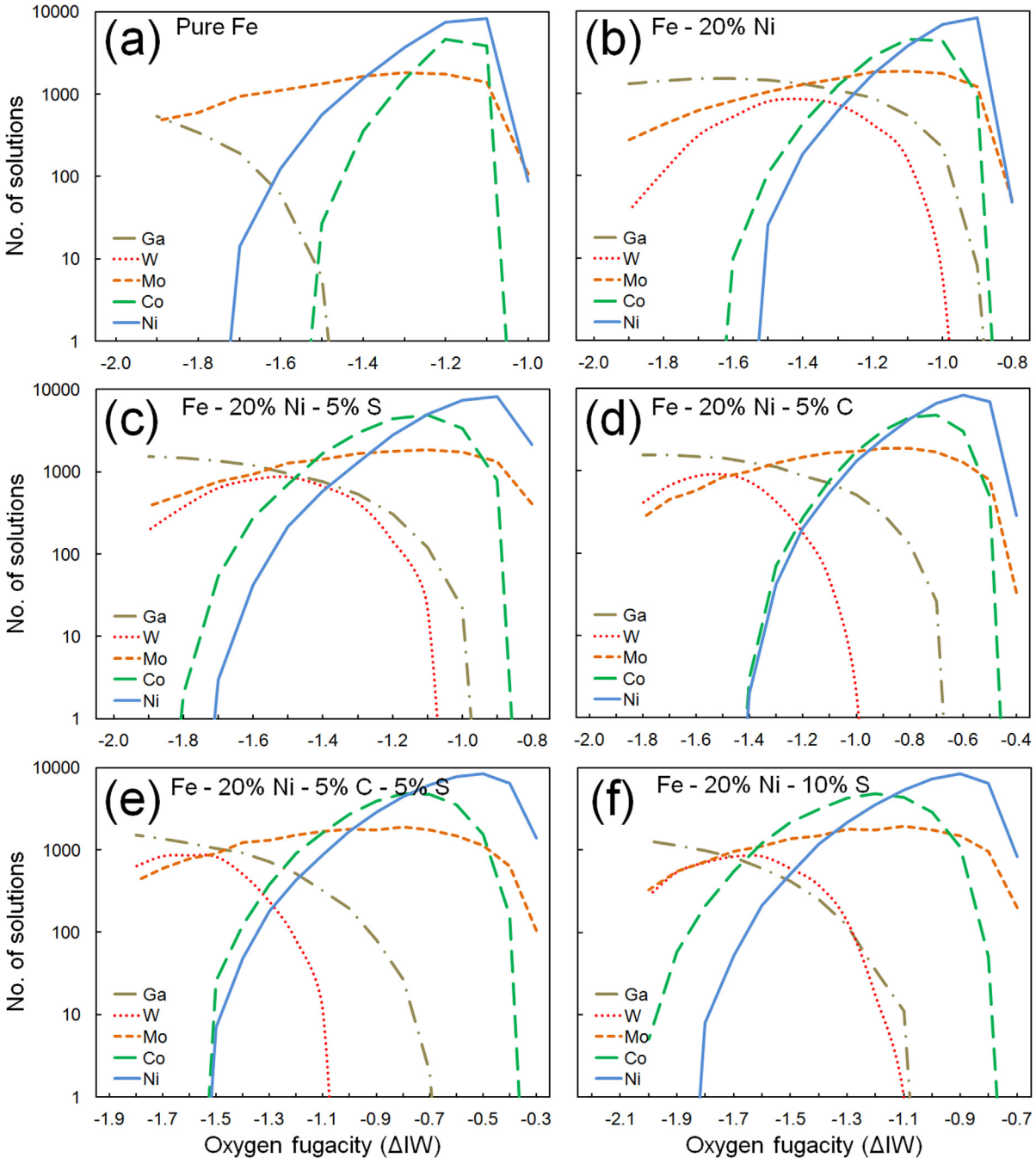

Fig. 8. Solution space as a function of fO_2 at 0.1 GPa, $T_{sol\text{-}liq}$ and assuming a CV bulk composition for (a) a pure Fe APB core, (b) an APB core with 20 wt.% Ni, (c) an APB core with 20 wt.% Ni and 5 wt.% S, (d) an APB core with 20 wt.% Ni and 5 wt.% C, (e) an APB core with 20 wt.% Ni, 5 wt.% C and 5 wt.% S and (f) an APB core with 20 wt.% Ni and 10 wt.% S.

iron abundance in the core, which in turn results in a wider range of fO_2 conditions under which an APB core could have formed, based on bulk APB Fe considerations. Applying the latter fO_2 range of APB core to the APB mantle depletions results in a solution space where the observed APB mantle depletions of all 5 elements considered can be simultaneously satisfied. For a 20 wt.% Ni-bearing Fe core, the observed depletions of all 5 elements considered here are confined to a fO_2 solution space of $\Delta IW = -1.25 \pm 0.30$ at 0.1 GPa (Fig. 8b). The boundaries of the solution space are determined by a lack of solutions for W at more oxidizing conditions, and the absence of solutions for Co and Ni at more reducing conditions (Fig. 8b).

We explored the effect of the presence of S and/or C on these results. Several examples for a Fe-rich APB core with 20 wt.% Ni and variable amounts of S and/or C are shown in Fig. 8c–f. Again, the lower bound of the solution space is

constrained by a lack of solutions for Ga and W, whereas the upper bound is defined by the absence of solutions for Ni and Co. We observe that addition of S and/or C to the APB core does not significantly change the previously derived fO_2 range of $\Delta IW = -1.25 \pm 0.30$. For example, an APB core with 20 wt.% Ni and 5 wt.% S is compatible with the considered mantle depletions of 5 siderophile elements at $\Delta IW = -1.40 \pm 0.35$, whereas the inferred fO_2 range is slightly more reducing for an APB core with 20 wt.% Ni and 10 wt.% S ($\Delta IW = -1.45 \pm 0.40$). The addition of C to the APB core results in similar inferred fO_2 estimates, but with a smaller range. An APB core with 20 wt.% Ni and 5 wt.% C is consistent with the siderophile element depletions at $\Delta IW = -1.20 \pm 0.25$. This is slightly more reducing for an APB core with 20 wt.% Ni, 5 wt.% C and 5 wt.% S ($\Delta IW = -1.30 \pm 0.25$).

Overall, our results constrain the fO_2 to $\Delta IW = -1.40 \pm 0.45$. This corresponds to an estimated APB core mass of $18 \pm 11\%$. The lowest core masses are expected for a FeNi core ($14 \pm 7\%$). However, the APB core is likely composed of significant amounts of S and/or C in addition to Fe and Ni, given its inferred building blocks. Consideration of a wider range of S and/or C contents in the APB core significantly increases the latter estimates to $21 \pm 8\%$. This range is further constrained to 20 ± 7 mass% if the fO_2 ranges recorded by pyroxene and olivine cores in angrites are considered (King et al., 2012; Shearer et al., 2016). We note that the 8% core mass and corresponding fO_2 range reported by Righter (2008) and Shirai et al. (2009) are close or within the lower and higher bound of our estimates, respectively. The slightly larger core mass derived here (and lower corresponding fO_2) are likely related to differences in the parameterizations, as the experimental database of metal-silicate partition coefficients used for our new parameterizations is expected to be significantly larger than used by Shirai et al. (2009).

For all scenarios, a FeNi core with or without light elements (S, C) results in a fO_2 range of the solution space inferred for APB core formation that is in excellent agreement with independent estimates of the redox state of the APB interior. We note that a Ni-rich APB core is also required from cosmochemical considerations that predict the APB formed from Ni-rich materials (e.g., CV chondrites). Evolution from reducing conditions to the more oxidizing conditions ($\Delta IW = +1$) required for angrite formation (e.g., Jurewicz et al., 1993; McKay et al., 1994) may have resulted from the presence of a C-bearing gas derived from graphite in the APB mantle, which became oxidized during magmatism (Shirai et al., 2009). This idea is supported by the presence of vesicles in some angrites (McCoy et al., 2006).

The inferred fO_2 range for APB core formation is slightly more oxidizing but similar to that derived for asteroid Vesta ($\Delta IW = -2.05 \pm 0.20$; Steenstra et al., 2016b). This is consistent with the hypothesis that the APB accreted in a similar region as Vesta. This hypothesis is substantiated by the similar spectral properties of angrites and some S and/or A-type asteroids which reside mostly in the inner asteroid belt (e.g., Burbine et al., 2001, 2006).

5. CONCLUSIONS

We present new experimental metal-silicate partitioning data for P, S, V, Cr, Mn, Co, Ni, Ge, Mo, and W obtained at pressures relevant for core formation in smaller-sized planetary bodies, such as Vesta, the angrite parent body (APB) and the Moon. We specifically explore the effect of silicate melt composition on D. We show that the metal-silicate partitioning of a wide range of siderophile elements is affected by changes in silicate melt composition, including Ni. We observe that the metal-silicate partitioning of P, Mo, and W is most strongly affected by the CaO content of the silicate melt, which agrees with previous work. The MgO content of silicate melts seems to have a similar, albeit smaller effect on their metal-silicate partition coefficients. We conclude that constraining silicate melt compositional dependencies of metal-silicate partition coefficients are in general complex, especially for elements such as Ni and Co for which the overall effect is small.

We combined our new experimental data with previous work to assess the range of X-fO_2 conditions that may have prevailed during metal-silicate segregation in the APB. We observe that the siderophile element depletions in angrites can be reconciled with a CV bulk composition and core formation occurring under mildly reducing conditions of $\Delta IW = -1.40 \pm 0.45$. This is in excellent agreement with independent fO_2 estimates based on pyroxene and olivine cores in angrites. Corresponding core mass is constrained to $18 \pm 11\%$ in this analysis. These results are independent of which parameterizations (including or excluding melt compositional terms) are used for Co and Ni.

ACKNOWLEDGEMENTS

We would like to thank three anonymous reviewers for their constructive criticisms of earlier versions of the manuscript and M. Humayun for the editorial handling. This study was funded by a Netherlands Organization for Scientific Research (N.W.O.) Vici grant to WvW and also partially funded by SFB TRR-170 (publ. No. 30).

APPENDIX A. SUPPLEMENTARY MATERIAL

Supplementary data associated with this article can be found, in the online version, at http://dx.doi.org/10.1016/j.gca.2017.05.034.

REFERENCES

Agee C. B., Li L., Shannon M. C. and Circone S. (1995) Pressure-temperature phase diagram for the Allende meteorite. *J. Geophys. Res.* **100**, 17725–177740.

Armstrong J. T. (1995) A package of correction programs for the quantitative electron microbeam X-ray analysis of thick polished materials, thin films, and particles. *Microbeam Anal.* **4**, 177–200.

Baghdadi B., Jambom A. and Barrat J.-A. (2015) Metamorphic angrite Northwest Africa 3164/5167 compared to magmatic angrites. *Geochim. Cosmochim. Acta* **168**, 1–21.

Ballhaus C., Laurenz V., Münker C., Fonseca R. O. C., Albarede F., Rohrbach A., Lagos M., Schmidt M. W., Jochum K.-P., Stoll G., Weis U. and Helmy H. M. (2013) The U/Pb ratio of the Earth's mantle – a signature of late volatile addition. *Earth Planet. Sci. Lett.* **362**, 237–245.

Blanchard I., Badro J., Siebert J. and Ryerson F. J. (2015) Composition of the core from gallium metal-silicate partitioning experiments. *Earth Planet. Sci. Lett.* **427**, 191–201.

Boyd F. R. and England J. L. (1960) Apparatus for phase-equilibrium measurements at pressures up to 50 kilobars and temperatures up to 1750 °C. *J. Geophys. Res.* **65**, 741–748.

Boujibar A., Andrault D., Bouhifd M. A., Bolfan-Casanova N., Devidal J.-L. and Trcera N. (2014) Metal-silicate partitioning of sulphur, new experimental and thermodynamic constraints on planetary accretion. *Earth Planet. Sci. Lett.* **391**, 42–54.

Borisov A. A. (2006) Experimental study of the effect of SiO_2 on Ni solubility in silicate melts. *Petrology* **14**(6), 530–539.

Borisov A. A. (2007) Experimental study of the influence of SiO_2 on the solubility of cobalt and iron in silicate melts. *Petrology* **15**(6), 523–529.

Burbine T. H., McCoy T. J. and Binzel R. P. (2001) Spectra of angrites and possible parent bodies. Lunar Planet. Sci. Conf. 32th, #1857 (abstr.).

Burbine T. H., McCoy T. J., Hinrichs J. L. and Lucey P. G. (2006) Spectral properties of angrites. *Meteorit. Planet. Sci.* **41**, 1139–1145.

Burkemper L. K., Agee C. B. and Garcia K. A. (2012) Constraints on core formation from molybdenum solubility in silicate melts at high pressure. *Earth Planet. Sci. Lett.* **335–336**, 95–104.

Campbell I. H., Naldrett A. J. and Roeder P. L. (1979) Nickel activity in silicate liquids: some preliminary results. *Can. Mineral.* **17**, 495–505.

Chabot N. L. and Agee C. B. (2003) Core formation in the Earth and Moon: new experimental constraints from V, Cr, and Mn. *Geochem. Cosmochim. Acta* **67**, 2077–2091.

Colson Russell O., Floden A. M., Haugen T. R., Malum K. M., Sawarynski M., Nermoe M. K. B., Jacobs K. E. and Holder D. (2005) Activities of NiO, FeO, and O^{2-} in silicate melts. *Geochim. Cosmochim. Acta* **69**, 3061–3073.

Corgne A., Keshav S., Wood B. J., McDonough W. F. and Fei Y. (2008) Metal-silicate partitioning and constraints on core composition and oxygen fugacity during Earth accretion. *Geochim. Cosmochim. Acta* **72**, 574–589.

Cottrell E., Walter M. J. and Walker D. (2009a) Metal-silicate partitioning of tungsten at high pressure and temperature: implications for equilibrium core formation in Earth. *Earth Planet. Sci. Lett.* **281**, 275–287.

Cottrell E., Walter M. J. and Walker D. (2009b) Erratum to: "Metal-silicate partitioning of tungsten at high pressure and temperature: implications for equilibrium core formation in Earth". *Earth Planet Sci. Lett.* **289**, 631–634.

Delano J. W. (1986) Pristine lunar glasses: criteria, data and implications. Proc. 16th Lunar Planet. Sci. Conf.. *J. Geophys. Res.* **91**, D201–D213.

Ehlers K., Grove T. L., Sisson T. W., Recca S. I. and Zervas D. A. (1992) The effect of oxygen fugacity on the partitioning of nickel and cobalt between olivine, silicate melt, and metal. *Geochim. Cosmochim. Acta* **56**, 3733–3743.

Gaetani G. A. and Grove T. L. (1997) Partitioning of moderately siderophile elements among olivine, silicate melt and sulphide melt: constraints on core formation in the Earth and Mars. *Geochim. Cosmochim. Acta* **61**, 1829–1846.

Greenwood R. C., Franchi I. A., Jambon A. and Buchanan P. C. (2005) Widespread magma oceans on asteroidal bodies in the early Solar System. *Nature* **435**, 916–918.

Griffin W. L., Powell W. J., Pearson N. J. and O'Reilly S. Y. (2008) GLITTER: datareduction software for laser ablation ICP-MS, in Sylvester, P., ed., Laser Ablation ICP-MS in the Earth Sciences: Current Practices and Outstanding Issues., Mineralogical Association of Canada. *Shourt Course Series* **40**, 308–311.

Hart S. R. and Davis K. E. (1978) Nickel partitioning between olivine and silicate melt. *Earth Planet. Sci. Lett.* **40**, 203–219.

Hillgren V. J., Drake M. J. and Rubie D. C. (1996) High pressure and high temperature metal-silicate partitioning of siderophile elements: the importance of silicate liquid composition. *Geochim. Cosmochim. Acta* **60**, 2257–2263.

Holzheid A., Palme H. and Chakraborty S. (1997) The activities of NiO, CoO and FeO in silicate melts. *Chem. Geol.* **139**, 21–38.

Holzheid A. and Palme H. (2007) The formation of eucrites: constraints from metal–silicate partition coefficients. *Meteorit. Planet. Sci.* **42**, 1817–1829.

Kegler P. H. and Holzheid A. (2011) Determination of the formal Ge-oxide species in silicate melts at oxygen fugacities applicable to terrestrial core formation scenarios. *Euro. J. Mineral.* **23**, 369–378.

Hutson M. L., Ruzicka A. M. and Mittlefehldt D. W. (2007) The case against mercury as the angrite parent body (APB). *70th Annual Met. Soc. Meet., Meteorit. Plan. Sci. Suppl.* **42**, 5238.

Jana D. and Walker D. (1997a) The influence of sulfur on partitioning of siderophile elements. *Geochim. Cosmochim. Acta* **61**, 5255–5277.

Jana D. and Walker D. (1997b) The influence of silicate melt composition on distribution of siderophile elements. *Earth Planet. Sci. Lett.* **150**, 463–472.

Jones J. H. (1984) Temperature and pressure independent correlation of olivine/liquid prtition coefficients and their application to trace element partitioning. *Contrib. Mineral. Petrol.* **88**, 126–132.

Jurewicz A. J. G., Mittlefehldt D. W. and Jones J. H. (1993) Experimental partial melting of the Allende CV and Murchison (CM) chondrites and the origin of asteroidal basalts. *Geochim. Cosmochim. Acta* **57**, 2123–2139.

Jurewicz A. J. G., Jones J. H., Mittlefehldt D. W. and Longhi, J. (2004) Devolatilized-Allende partial melts as an analog for primitive angrite magmas. Lunar Planet. Sci. XXXV #1417 (abstr.).

Kegler P. A., Holzheid D. J., Frost D., Rubie C., Dohmen R. and Palme H. (2008) New Ni and Co metal-silicate partitioning data and their relevance for an early terrestrial magma ocean. *Earth Planet. Sci. Lett.* **268**, 28–40.

Keil K. (2012) Angrites, a small but diverse suite of ancient, silica-undersaturated volcanic-plutonic mafic meteorites, and the history of their parent asteroid. *Chem. Erde* **72**(3), 191–218.

Killburn M. R. and Wood B. J. (1997) Metal-silicate partitioning and the incompatibility of S and Si during core formation. *Earth Planet. Sci. Lett.* **152**, 139–148.

King P. L., Sutton S. R., Spilde M. N., Wirick S., Lanzirotti A. and Agee C.B. (2012) Redox history of early solar system planetesimals recorded in the D'Orbigny Angrite. Lunar Planet. Sci. 43rd, #2436 (abstr.).

Kiseeva E. S. and Wood B. J. (2013) A simple model for chalcophile element partitioning between silicate and sulphide liquids with geochemical applications. *Earth Planet. Sci. Lett.* **383**, 68–81.

Kleine T., Hans U., Irving A. J. and Bourdon B. (2012) Chronology of the angrite parent body and implications for core formation in protoplanets. *Geochim. Cosmochim. Acta* **84** (1), 186–203.

Mavrogenes J. A. and O'Neill H. S. C. (1999) The relative effects of pressure, temperature and oxygen fugacity on the solubility of

sulphide in mafic magmas. *Geochim. Cosmochim. Acta* **63**, 1173–1180.
McCoy T. J., Ketcham R. A., Wilson L., Benedix G. K., Wadhwa M. and Davis A. M. (2006) Formation of vesicles in asteroidal basaltic meteorites. *Earth Planet. Sci. Lett.* **246**, 102–108.
McDade P., Wood B. J., van Westrenen W., Brooker R., Gudmundsson G., Soulard H., Najorka J. and Blundy J. (2002) Pressure corrections for a selection of piston-cylinder cell assemblies. *Mineral. Mag.* **66**(6), 1021–1028.
McKay G., Le L., Wagstaff J. and Crozaz G. (1994) Experimental partitioning of rare earth elements and strontium: constraints on petrogenesis and redox conditions during crystallization of Antarctic angrite Lewis Cliff 86,010. *Geochim. Cosmochim. Acta* **58**, 2911–2919.
Mysen B. O., Virgo D. and Seifert F. A. (1982) The structure of silicate melts: implications for chemical and physical properties of natural magmas. *Rev. Geophys. Space Phys.* **20**, 353–383.
Mysen B. O. and Virgo D. (1985) Iron-bearing silicate melts: relations between pressure and redox equilibria. *Phys. Chem. Minerals* **12**, 191–200.
Mungall J. E. and Brenan J. M. (2014) Partitioning of platinum-group elements and Au between sulphide liquid and basalt and the origins of mantle-crust fractionation of the chalcophile elements. *Geochim. Cosmochim. Acta* **125**, 265–289.
Newsom H. E. and Drake M. J. (1982) The metal content of the eucrite parent body: constraints from the partitioning behaviour of tungsten. *Geochim. Cosmochim. Acta* **46**, 2483–2489.
Newsom H. E. and Drake M. J. (1983) Experimental investigations of the partitioning of phosphorus between metal and silicate phases: implications for the Earth, Moon and eucrite parent body. *Geochim. Cosmochim. Acta* **47**, 93–100.
Newsom H. E. (1995) Composition of the solar system, planets, meteorites, and major terrestrial reservoirs. In *Global Earth Physics: A Handbook of Physical Constants, AGU Reference Shelf*, vol. 1 (ed. T. J. Ahrens). American Geophysical Union, Washington, D.C., pp. 159–189.
O'Neill H. S. C. and Eggins S. M. (2002) The effect of melt composition on trace element partitioning: an experimental investigation of the activity coefficients of FeO, NiO, CoO, MoO_2 and MoO_3 in silicate melts. *Chem. Geol.* **186**, 151–181.
O'Neill H. S. C., Berry A. J. and Eggins S. M. (2008) The solubility and oxidation state of tungsten in silicate melts: Implications for the comparative chemistry of W and Mo in planetary differentiation processes. *Chem. Geol.* **255**, 346–359.
Palme H., Kegler P., Holzheid A., Frost A. and Rubie D. J. (2011) Comment on "Prediction of metal-silicate partition coefficients for siderophile elements: An update and assessment of PT conditions for metal-silicate equilibrium during accretion of the Earth" by Righter K. (2011), Earth Planet. Sci. Lett. 304, 158–167. *Earth Planet. Sci. Lett.* **312**, 516–518.
Peach C. L. and Mathez E. A. (1993) Sulfide melt–silicate melt distribution coefficients for nickel and iron and implications for the distribution of other chalcophile elements. *Geochim. Cosmochim. Acta* **57**, 3013–3021.
Pretorius E. B. and Muan A. (1992) Activity of nickel(II) oxide in silicate melts. *J. Am. Ceram. Soc.* **75**(6), 1490–1496.
Pringle E. A., Moynier F., Savage P. S., Badro J. and Barrat J.-A. (2014) Silicon isotopes in angrites and volatile loss in planetesimals. *Proc. Nat. Acad. Sci.* **111**, 17029–17032.
Putter R., Steenstra E. S., Seegers A. X., Lin Y. H., Matveev S., Berndt J., Rai N., Klemme S. and van Westrenen W. (2017) Effects of fO2 on metal-silicate partitioning of refractory and moderately volatile siderophile elements: implications for the Si content of Mercury's core. 48th Lunar Planet. Sci. Conf. #1055 (abstr.).
Rai N. and van Westrenen W. (2013) Core-mantle differentiation in Mars. *J. Geophys. Res.: Planets* **118**, 1195–1203.
Rai N. and van Westrenen W. (2014) Lunar core formation: new constraints from metal-silicate partitioning of siderophile elements. *Earth Planet. Sci. Lett.* **388**, 343–352.
Riches A. J. V., Day J. M. D., Walker R. J., Simonetti A., Liu Y., Neal C. R. and Taylor L. A. (2012) Rhenium-osmium isotope and highly-siderophile-element abundance systematic of angrite meteorites. *Earth Planet. Sci. Lett.* **353–354**, 208–218.
Righter K. and Drake M. J. (1996) Core formation in the Earth's Moon, Mars, and Vesta. *Icarus* **124**, 513–529.
Righter K., Drake M. J. and Yaxley G. (1997) Prediction of siderophile element metal-silicate partition coefficients to 20 GPa and 2800 °C: the effect of pressure, temperature, fO2 and silicate and metallic melt composition. *Phys. Earth Planet. Inter.* **100**, 115–134.
Righter K. and Drake M. J. (2000) Metal/silicate equilibrium in the early Earth – New constraints from the volatile moderately siderophile elements Ga, Cu, P, and Sn. *Geochim. Cosmochim. Acta* **64**, 3581–3597.
Righter K. (2003) Metal-silicate partitioning of siderophile elements and core formation in the early earth. *Annu. Rev. Earth Planet. Sci.* **31**, 74–135.
Righter K. (2008) Siderophile element depletion in the Angrite Parent Body (APB) mantle: due to core formation? Lunar and Planet Sci. Conf. XXXIX #1936 (abstr.).
Righter K., Pando K. M., Danielson L. and Lee C. (2010) Partitioning of Mo, P and other siderophile elements (Cu, Ga, Sn, Ni Co, Mn, Cr, V and W) between metal and silicate melt as a function of temperature and silicate melt composition. *Earth Planet. Sci. Lett.* **291**, 1–9.
Righter K. (2011a) Prediction of metal-silicate partition coefficients for siderophile elements: an update and assessment of PT conditions for metal-silicate equilibrium during accretion of the Earth. *Earth Planet. Sci. Lett.* **304**, 158–167.
Righter K. (2011b) Reply to the Comment by Palme et al. on "Prediction of metal-silicate partition coefficients for siderophile elements: an update and assessment of PT conditions for metal-silicate equilibrium during accretion of the Earth. *Earth Planet. Sci. Lett.* **312**, 519–521.
Righter K., King C., Danielson K., Pando K. and Lee C. T. (2011) Experimental determination of the metal/silicate partition coefficient of Germanium: implications for core and mantle differentiation. *Earth Planet. Sci. Lett.* **304**, 379–388.
Righter K., Danielson L. R., Pando K. M., Williams J., Humayun M., Hervig R. L. and Sharp T. G. (2015) Highly siderophile element (HSE) abundances in the mantle of Mars are due to core formation at high pressure and temperature. *Meteorit. Planet. Sci.* **50**, 604–631.
Righter K., Danielson L. R., Pando K. M., Shofner G. A., Sutton S. R., Newville M. and Lee C.-T. (2016) Valence and metal/silicate partitioning of Mo: implications for conditions of Earth accretion and core formation. *Earth Planet. Sci. Lett.* **437**, 89–100.
Rose-Weston L., Brenan J. M., Fei Y., Secco R. A. and Frost D. J. (2009) Effect of pressure, temperature, and oxygen fugacity on the metal-silicate partitioning of Te, Se, and S: implications for earth differentiation. *Geochim. Cosmochim. Acta* **73**, 4598–4615.
Sanloup C., van Westrenen W., Dasgupta R., Maynard-Casely H. and Perrillat J.-P. (2011) Compressibility change in iron-rich melt and implications for core formation models. *Earth Planet. Sci. Lett.* **306**, 118–122.
Schiller M., Baker J. A. and Bizzarro M. (2010) ^{26}Al-^{26}Mg dating of asteroidal magmatism in the young solar system. *Geochim. Cosmochim. Acta* **74**(16), 4844–4864.

Schiller M., Connelly J. N., Glad A. C., Mikouchi T. and Bizzarro M. (2015) Early accretion of protoplanets inferred from a reduced inner solar system 26Al inventory. *Earth Planet. Sci. Lett.* **420**, 45–54.

Seegers A. X., Steenstra E. S., Putter R., Lin Y. H., Berndt J., Matveev S., Rai N., Klemme S. and van Westrenen W. (2017) The effects of Si and fO2 on the metal-silicate partitioning of volatile siderophile elements: implications for the Se/Te systematics of the bulk silicate Earth. 48th Lunar Planet. Sci. Conf. #1053 (abstr.).

Seifert S., O'Neill H. S. C. and Brey G. (1988) The partitioning of Fe, Ni and Co between olivine, metal and basaltic liquid: an experimental and thermodynamic investigation, with application to the composition of the Lunar core. *Geochim. Cosmochim. Acta* **52**, 603–616.

Sharp M., Righter K. and Walker R. J. (2015) Estimation of trace element concentrations in the lunar magma ocean using mineral- and metal-silicate melt partition coefficients. *Meteorit. Planet. Sci.* **50**, 733–758.

Shearer C. K., Bell A. S., Burger P. V., Papike J. J., Jones J. and Le L. (2016) The Cr redox record of fO2 variation in angrites. Evidence for redox conditions of angrite petrogenesis and parent body. Lunar Planet. Sci. Conf. 47th, #1370 (abstr.).

Shirai N., Humayun M. and Righter K. (2009) Analysis of moderately siderophile elements in angrites: implications for core formation of the angrite parent body. Lunar Planet. Sci. Conf. 40th, #2122 (abstr.).

Siebert J., Corgne A. and Ryerson F. J. (2011) Systematics of metal-silicate partitioning for many siderophile elements applied to Earth's core formation. *Geochim. Cosmochim. Acta* **75**, 1451–1489.

Steenstra E. S., Rai N., Knibbe J. S., Lin Y. H. and van Westrenen W. (2016a) New geochemical models of core formation in the Moon from metal-silicate partitioning of 15 siderophile elements. *Earth Planet. Sci. Lett.* **441**, 1–9.

Steenstra E. S., Knibbe J. S., Rai N. and van Westrenen W. (2016b) Constraints on core formation in Vesta from metal-silicate partitioning of siderophile elements. *Geochim. Cosmochim. Acta* **177**, 48–61.

Steenstra E. S., Dankers D., Lin Y. H., Rai N., Berndt J., and van Westrenen W. (2016c) Metal-silicate partitioning of S, Mn, Cr, Ni, As, Se, Cd, In, Sb, Te, and Pb at high pressure and temperature and its relevance for core formation in the Moon, asteroid Vesta and the angrite parent body. Lunar Planet. Sci. Conf. 47th #1851 (abstr.).

Steenstra E. S., Lin Y. H., Rai N., Jansen M. and van Westrenen W. (2017a) Carbon as the dominant light element in the lunar core. *Am. Miner.* **102**, 92–97. http://dx.doi.org/10.2138/am-2017-5727.

Steenstra E.S., Putter R., Seegers, A. X., Lin Y. H. and van Westrenen W. (2017b) Significant non-linear pressure effects on interaction coefficients of siderophile elements in FeSi alloys: Implications for geochemical models of core formation in the Earth. Lunar Planet. Sci. Conf. 48th #1050 (abstr.).

Sugiura N., Miyazaki A. and Yanai K. (2005) Widespread magmatic activities on the angrite parent body at 4562 Ma ago. *Earth Planets Space* **57**, e13–e16.

Takahashi E. (1978) Partitioning of Ni^{2+}, Co^{2+}, Fe^{2+}, Mn^{2+}, and Mg^{2+} between olivine and silicate melts: compositional dependence of partition coefficient. *Geochim. Cosmochim. Acta* **42**, 1829–1844.

Thibault Y. and Walter M. J. (1995) The influence of pressure and temperature on the metal-silicate partition coefficients of nickel and cobalt in a model C1 chondrite and implications for metal segregation in a deep magma ocean. *Geochim. Cosmochim. Acta* **59**, 991–1002.

Tuff J., Wood B. J. and Wade J. W. (2011) The effect of Si on metal-silicate partitioning of siderophile elements and implications for the conditions of core formation. *Geochim. Cosmochim. Acta* **75**, 673–690.

van Achterbergh E., Ryan C. G., Jackson S. E. and Griffin W. L. (2001) Data reduction software for LA-ICP-MS: appendix. In: P. J. Sylvester (Ed.), Laser Ablation-ICP Mass Spectrometry in the Earth Sciences: Principles and Applications (vol. 29, 239–243). Ottawa: Mineralog. Assoc. Canada (MAC) Short Course Series.

van Kan Parker M., Mason P. R. D. and van Westrenen W. (2011) Experimental study of trace element partitioning between lunar orthopyroxene and anhydrous silicate melt: effects of lithium and iron. *Chem. Geol.* **285**, 1–14.

van Westrenen W., Steenstra E. S., Knibbe J. S., Lin Y. H., Rai N. and Berndt J. (2016) Metal-silicate partitioning of P, V Co, Mo, Ge, and W and core formation in the angrite parent body. Lunar Planet. Sci. Conf. 47th, #1630 (abstr.).

Wade J. and Wood B. J. (2005) Core formation and the oxidation state of the Earth. *Earth Planet. Sci. Lett.* **236**, 78–95.

Wood B. J., Wade J. and Kilburn M. R. (2008) Core formation and the oxidation state of the Earth: additional constraints from Nb, V and Cr partitioning. *Geochim. Cosmochim. Acta* **72**, 1415–1426.

Wade J., Wood B. J. and Tuff J. (2012) Metal-silicate partitioning of Mo and W at high pressures and temperatures: evidence for late accretion of sulphur to the Earth. *Geochim. Cosmochim. Acta* **85**, 58–74.

Walter M. J., Newsom H. E., Ertel W. and Holzheid A. (2000) Siderophile Elements in the Earth and Moon: Metal/Silicate Partitioning and Implications for Core Formation. In: Origin of the Earth and Moon, edited by R.M. Canup and K. Righter and 69 collaborating authors. Tucson: University of Arizona Press., p. 265–289.

Walter M. J. and Cottrell E. (2013) Assessing uncertainty in geochemical models for core formation in Earth. *Earth Planet Sci. Lett.* **365**, 165–176.

Warren P. H., Taylor G. J., Keil K., Shirley D. N. and Wasson J. T. (1983) Petrology and chemistry of two "large" granite clasts from the moon. *Earth Planet. Sci. Lett.* **64**, 175–185.

Weiss B. P., Berdahl J. S., Elkins-Tanton L., Stanley S., Lima E. A. and Carporzen L. (2008) Magnetism on the angrite parent body and the early differentiation of planetesimals. *Science* **322**, 71–716.

Wood B. J. and Wade J. (2013) Activities and volatilities of trace components in silicate melts: a novel use of metal-silicate partitioning data. *Contrib. Mineral. Petrol.* **166**, 911–921.

Wood B. J., Kiseeva E. S. and Mirolo F. J. (2014) Accretion and core formation: the effects of sulfur on metal-silicate partition coefficients. *Geochim. Cosmochim. Acta* **145**, 248–267.

Associate Editor: Munir Humayun